JOURNAL OF MATERIALS SCIENCE 38 (2003) 4087 – 4113

Probabilistic Weibull behavior and mechanical properties of MEMS brittle materials

O. M. JADAAN
University of Wisconsin-Platteville, College of Engineering, Mathematics, and Science, Platteville, WI 53818, USA

N. N. NEMETH
NASA Glenn Research Center, Cleveland, OH 44135, USA

J. BAGDAHN
Fraunhofer Institute for Mechanics of Materials, Head Micromechanical Components and Nanotechnologies, Germany

W. N. SHARPE, JR.
Department of Mechanical Engineering, The Johns Hopkins University, Baltimore, MD 21218-2681, USA

The objective of this work is to present a brief overview of a probabilistic design methodology for brittle structures, review the literature for evidence of probabilistic behavior in the mechanical properties of MEMS (especially strength), and to investigate whether evidence exists that a probabilistic Weibull effect exists at the structural microscale. Since many MEMS devices are fabricated from brittle materials, that raises the question whether these miniature structures behave similar to bulk ceramics. For bulk ceramics, the term Weibull effect is used to indicate that significant scatter in fracture strength exists, hence requiring probabilistic rather than deterministic treatment. In addition, the material's strength behavior can be described in terms of the Weakest Link Theory (WLT) leading to strength dependence on the component's size (average strength decreases as size increases), and geometry/loading configuration (stress distribution). Test methods used to assess the mechanical properties of MEMS, especially strength, are reviewed. Four materials commonly used to fabricate MEMS devices are reviewed in this report. These materials are polysilicon, single crystal silicon (SCS), silicon nitride, and silicon carbide. © *2003 Kluwer Academic Publishers*

1. Overview of probabilistic design methodology for brittle materials

MEMS technology, which can integrate sensors, actuators, and electronics on the same silicon chip, can be used in such applications as sensors to detect ice on airplane wings, flexible heat flux sensors capable of determining heat flux at multiple locations on a turbine blade [1], arrays of microcilia actuators used in docking systems for small spacecrafts such as miniature satellites [2], microjet actuators for turbine combustion applications, micro-power generators, and distributed networks of acoustic, pressure, and temperature sensors for unmanned aerial vehicle (UAV) situational awareness. Other very popular MEMS applications include accelerometers to deploy air bags, pressure sensors in "smart" tires, and Digital Micromirror Devices (DMD) used in the digital projection arena.

MEMS devices are typically made from brittle materials such as silicon. The mechanical properties and inherent defects of such microdevices can vary significantly as a function of the processing conditions. For deposited films, small changes in the deposition temperature, pressure and gas flow rates can induce changes in the number of point defects, dislocations, grain boundaries and thermal mismatches between the as-deposited film and substrate, which, in turn can effect the crystallinity, elastic modulus, and residual stress. The fracture strength of MEMS devices is also affected by surface defects and resultant surface roughness from the manufacturing process. Such variability can directly impact the failure modes and in turn the reliability of MEMS devices. Therefore, a consistent probabilistic methodology for assessing the mechanical reliability of brittle MEMS structures is needed.

When using brittle materials in structural applications, a penalty is paid in that these materials typically exhibit low fracture toughness. This inherent undesirable property must be considered when designing components. Lack of ductility (i.e., lack of fracture toughness) leads to low strain tolerance and large variations in observed fracture strength. When a load is applied, the absence of significant plastic deformation or microcracking causes large stress concentrations to occur at microscopic flaws. These flaws are unavoidably present as a result of fabrication or in-service environmental factors.

Traditional material failure analyses employing a deterministic approach, where failure is assumed to occur when some allowable stress level or equivalent stress is exceeded, are not adequate for brittle material component design. Such phenomenological failure theories are reasonably successful when applied to ductile materials. However, since analysis of failure in ceramic components is governed by the observed scatter in strength, statistical design approaches must be used to accurately reflect the stochastic physical phenomena that determine material fracture response. Accounting for these phenomena requires a change in philosophy on the design engineer's part that leads to a reduced focus on the use of safety factors in favor of reliability analyses. However, the reliability approach demands that the design engineer must tolerate a finite risk of unacceptable performance. This risk of unacceptable performance is identified as a component's probability of failure (or alternatively, component reliability). The primary concern of the engineer is to minimize this risk in an economical manner.

Probabilistic component design involves predicting the probability of failure for a thermomechanically and/or electrostatically loaded component from simple specimen strength data. Typically these experiments are performed using many geometrically simple flexural or tensile test specimens. A static, dynamic, or cyclic load is applied to each specimen until fracture. Statistical strength and fatigue parameters are then determined from these data. Using these statistical parameters, a probabilistic reliability model, and the results (i.e., stress and temperature distributions) obtained from a finite element analysis, the probability of failure for a component with complex geometry and loading can be predicted.

Designing brittle components, including MEMS, to survive in severe loading applications involves the disciplines of statistics and fracture mechanics. Successful application of advanced ceramics depends on proper characterization of material properties and the use of a probabilistic brittle material design methodology. The NASA CARES/*Life* integrated design software [3] combines multidisciplinary research—in the areas of fracture analysis, probabilistic modeling, and brittle structure design—to determine the failure probability of monolithic ceramic components. The CARES/*Life* software describes the probabilistic nature of material strength using the Weibull cumulative distribution function [4]. For uniaxially stressed components the 2-parameter Weibull distribution for surface residing flaws describes the component failure probability, P_{f}, as

$$P_{\mathrm{f}} = 1 - \exp\left[-\frac{1}{\sigma_0^{\mathrm{m}}}\int_A \sigma(x, y, z)^{\mathrm{m}}\,\mathrm{d}A\right] \qquad (1)$$

where A is the surface area, $\sigma(x, y, z)$ is the uniaxial stress at a point location on the body surface, and m and σ_0 are the Weibull modulus and scale parameter of the Weibull distribution, respectively. The Weibull modulus is a measure of the dispersion of strength while the scale parameter is the strength of a unit area of material at 63.21% probability of failure. An analogous equation based on volume can be shown for flaws residing within the body of the component. The Weibull equation is based on the weakest-link theory (WLT). The WLT assumes that the structure is analogous to a chain with many links. Each link may have a different limiting strength. When a load is applied to the structure such that the weakest link fails, then the structure fails. The effect of multiaxial stresses on reliability is predicted by using either the principle of independent action (PIA), [5, 6] the Weibull normal stress averaging method (NSA), [7] or the Batdorf theory [8, 9]. For the PIA model the reliability of a component under multiaxial stresses is the product of the reliability of the individual principal stresses acting independently, which for surface distributed flaws is

$$P_{\mathrm{f}} = 1 - \exp\left[-\frac{1}{\sigma_0^{\mathrm{m}}}\int_A \sum_{i=1}^{2}\sigma_i(x, y, z)^{\mathrm{m}}\,\mathrm{d}A\right] \qquad (2)$$

where i is the individual principal stress component. The NSA method involves the integration and averaging of tensile normal stress components evaluated about all possible orientations and locations. This approach is a special case of the more general Batdorf theory and assumes the material to be shear insensitive. The Batdorf theory combines the weakest link theory and linear elastic fracture mechanics (LEFM). Conventional fracture mechanics analysis requires that both the size of the critical crack and its orientation relative to the applied loads determine the fracture stress. The Batdorf theory includes the calculation of the combined probability of the critical flaw being within a certain size range and being located and oriented so that it may cause fracture. The probability of failure for a ceramic component using the Batdorf model for surface flaws can be expressed as

$$P_{\mathrm{f}} = 1 - \exp\left[-\frac{k_{\mathrm{B}}}{\pi}\int_A \int_0^{\pi} \left\{\sigma_{Ieqc_{\max}}(\omega)\right\}^{\mathrm{m}}\,\mathrm{d}\alpha\,\mathrm{d}A\right] \qquad (3)$$

where A is the surface area, ω is the arc length of an angle α projected onto a unit radius semi-circle in principal stress space containing all of the crack orientations for which the effective stress is greater than or equal to the critical crack propagation stress, k_{B} and m are the Weibull parameters describing the material, and $\sigma_{Ieqc_{\max}}$ is far-field equivalent maximum normal stress. Equation 3 can be shown to reduce to a simple 2-parameter Weibull distribution.

2. Mechanical test methods for thin film microspecimens

It is necessary to evaluate the mechanical properties at the same microscale level as the MEMS devices in order to reliably design them and predict their performance. In general, microspecimens used to evaluate the mechanical properties of MEMS are similar to macrospecimens used to evaluate the bulk mechanical properties of materials. However, testing at the microscale present significant new challenges such as gripping and measuring the mechanical response for these microspecimens.

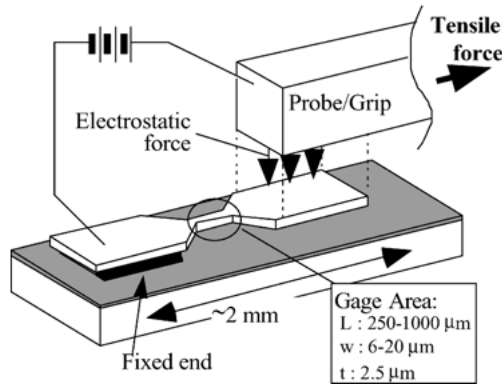

Figure 1 Tensile testing using electrostatic force grip [10, 11].

Bulk material properties do not extrapolate to the microscale level because of the increase of surface to volume ratio, and presence of intrinsic stresses (lattice and thermal mismatch stresses) due to fabrication techniques. A brief review of the most popular test methods used by investigators to characterize the micromechanical behavior of thin films follows.

2.1. Tensile specimen testing

The tensile test is a well-known and popular technique for evaluating the mechanical properties of bulk materials. The load-deflection diagram can be used to directly extract important properties such as fracture strength, elastic modulus, and ductility. When transverse strain is measured, then Poisson's ratio can also be computed. Hence, it is no wonder that the tensile specimen is also used to evaluate the mechanical properties of thin films at the microscale level. Several microtensile techniques exist for mounting and extracting relevant data. Some of these techniques will briefly be presented next. For further information, the reader should consult the relevant references.

Tsuchiya and coworkers [10, 11] at Toyota developed a tensile tester based on electrostatic-force gripping system (Fig. 1). The tester was constructed within a Scanning Electron Microscope (SEM) chamber for *in situ* observation. Tensile specimens with lengths between 30 to 1000 μm, and widths between 2 to 20 μm were tested [11–13]. In their setup, the specimen is fabricated on a silicon wafer with one large free end and one end attached to the silicon substrate. The free end of the specimen is fixed to a flat probe by electrostatic force, which is controlled through the applied voltage. Subsequently, a tensile force is applied to the specimen until it fractures. Friction force holds the surfaces of the probe and the specimen together. The applied tensile force is monitored with a strain gauge at the probe, while the displacement is measured with a strain gauge located on the precise stage where the specimen is placed.

At Johns Hopkins University, Sharpe and coworkers developed a microtensile test technique that is also based on electrostatic gripping [14–16]. Fig. 2 shows the tensile specimen and a schematic representation of the test setup. In their technique, a die (1 cm^2) containing 16 microtensile specimens was glued to a mount, which was attached to a five-axis piezoelectric stage. The large paddle free ends of the specimens were gripped with an electrostatic probe. The probe is brought close to the specimen and when the power supply is turned on, the paddle is attracted to it. Subsequently, the five-axis piezoelectric stage is used to position the specimen relative to the probe. A single-axis piezoelectric stage is used to pull the specimen, and a capacitance-based displacement probe measures the overall displacement of the system. The fracture stress and the modulus of narrow specimens could then be determined from the force-displacement data. Wide specimens lend themselves to direct strain measurement via laser interferometery. This is done by depositing two closely spaced reflective gage markers on the specimen and using the laser to correlate strain to interference fringes.

At Sandia National Lab, a pull-tab tensile specimen [17–19], shown in Fig. 3, is used to characterize the tensile strength and elastic modulus of thin films. The specimen has a freely moving pivot and a pull-tab. The specimen's gage length, which can vary between 15 and 1000 μm, connects the pull-tab and the pivot together. Because earlier generation specimens failed outside the gage length, recent generation samples were redesigned

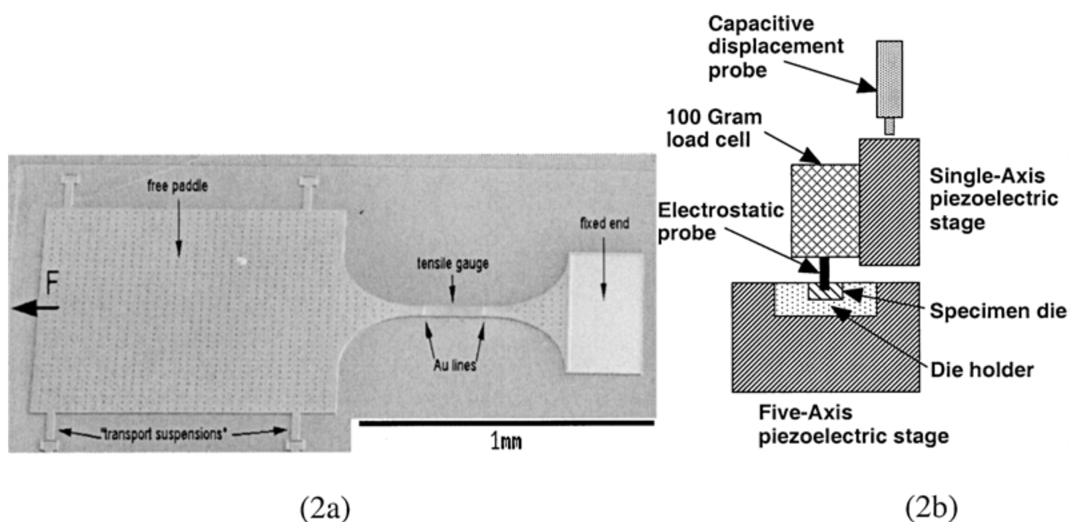

Figure 2 SEM image of the Johns Hopkins test specimen (2a), and a Schematic representation of the test setup (2b).

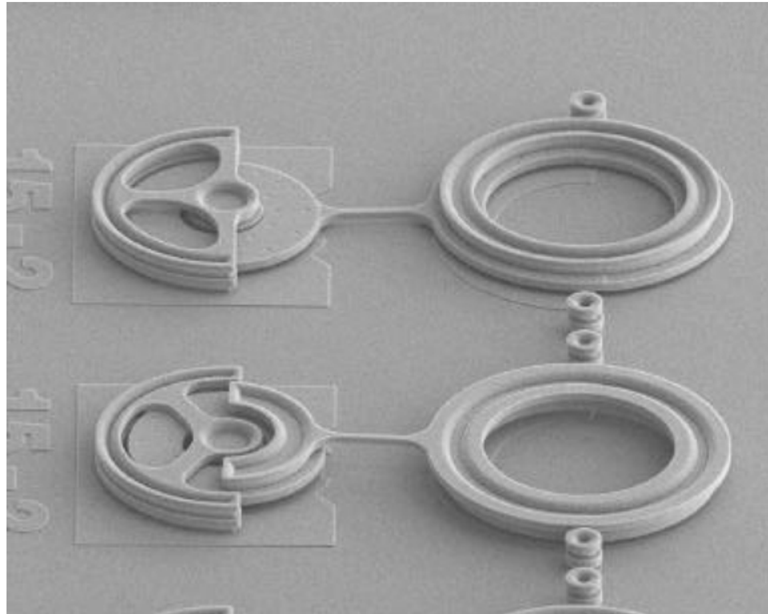

Figure 3 Sandia National Lab pull-tab microtensile specimen (latest design generation).

to have larger fillet radii and more robust pivots. Testing involves engaging the pull-tab end of the sample with a 35 μm diameter flat-tipped diamond nanoindentor [19]. The tip is centered within the pull-tab and pulled to apply the tensile force. Data acquisition system is used to record the force-displacement data, which subsequently is used to compute the stress-strain response. This test technique has a load accuracy of ± 50 μN, displacement accuracy of ± 50 μm, and can be used to test 20–30 samples per day.

In Sweden, Greek and coworkers [20, 21] devised a similar specimen configuration to that used at Sandia where a probe is inserted in the ring at one end of the tensile specimen and pulled. The testing unit consists of an arm with a probe, a voltage-driven piezoelectric actuator and a strain gauge force sensor. The strain gauges are made from silicon. This test has the added advantage of being performed *in situ* within a SEM. A computer-based control and data acquisition system is used to slowly raise the voltage applied to the actuator, while sampling amplified signals from the force sensor. After fracture the specimen's cross section is measured by SEM and the tensile strength is computed.

Other microtensile test set-ups were also developed and presented in the literature. These include the on-chip tensile test developed by Ando *et al.* [22], and the microtensile test using magnetic-solenoid force actuator developed by Ding *et al.* [23].

2.2. Beam specimen testing

Investigators characterizing the micromechanical properties of thin films have also used beam testing, and specifically the cantilever beam configuration. Like the tensile specimen, a uniaxial but not uniform stress state exists in a bent beam, hence allowing for simple and effective means for studying the mechanical behavior of materials. Because the maximum stress occurs at the beam's surface, this specimen configuration permits characterization of the material's surface flaws where failure is likely to initiate. Another advantage to the beam test configuration, compared to other structures that tend to shatter upon fracture, is that the location and mode of failure is preserved. Even tensile specimens, especially long ones, tend to shatter at the moment of failure making discerning the failure mode and location impossible to determine. For reliability analysis purposes it is important to determine the location and cause of failure.

Wilson *et al.* [24, 25], at Hewlett Packard laboratories, used microcantilever beams to characterize the strength and elastic modulus of single crystal silicon (SCS). In their facility, arrays of cantilever beams were fabricated using bulk micromachining on {100} silicon wafers. Depending on the fabrication method, beams can be aligned along desired crystallographic directions. Wilson *et al.* fabricated their microcantilever beams along the $\langle 100 \rangle$ direction. Reactive ion etching was used for the topside to define the length and width of the beam, while anisotropic etching (KOH) was applied to the bottom side to define the beam thickness. These double-sided etching procedures yielded arrays of cantilever beams suspended in cavities penetrating the total wafer thickness. The beams produced all had the same width of 200 μm, lengths varying from 350 to 750 μm, and thicknesses from 16 to 30 μm. To test a microcantilever beam on a wafer, the load pin is brought close to the beam using the micrometer above the force transducer. Subsequently the wafer is displaced upward causing the beam to deflect downward. The magnitude of the force is measured with a force transducer, while the displacement is measured using a micro-displacement gauge. Using this test method, the load-deflection curve and fracture force are obtained for each beam tested. Wilson *et al.* subsequently simulated the test configuration using FEA, taking into account anisotropy, to compute the fracture stresses corresponding to the measured fracture forces.

Johansson *et al.* [26], at Uppsala University in Sweden, fracture tested SCS microcantilever beams

in situ in a SEM. Beams of various sizes and orientations (⟨100⟩ and ⟨110⟩) were fabricated on {100} wafers. The SEM is well suited for monitoring the instrumentation before, and after testing. It also enables the application of loads under well-controlled conditions. In addition, the resulting fractures can be directly studied in vacuum, without extra handling. The silicon cantilever beams were manufactured using two different micromachining techniques; one producing rounded corners and the other sharp corners. The central component of the *in situ* equipment is an X-Y table in which the specimen is fixed. The specimen table can be moved sideways for lateral positioning. The normal force is applied by means of a stylus positioned at the end of a lever, and is measured by a strain gauge adhered to the lever. Johansson *et al.* used simple beam theory to compute the fracture stresses. Ericson and Schweitz [27] also used this same *in situ* testing technique to characterize the mechanical properties of SCS.

Jones *et al.* [28] devised a microcantilever test methodology and applied it to characterize polysilicon. The structure used in their work allows a large number of specimens to be tested to failure in a reasonable time. However, their test device does not provide a direct determination of fracture stress. Rather, the strain at failure is determined, from which the associated stress can be computed using the elastic modulus. The central element of Jones *et al.*'s test setup is a shuttle tethered to the substrate by a folded flexure. Attached to the shuttle is an array of cantilever beams that are bent as the shuttle is displaced in-plane by a probe at a rate of 0.05 μm/s. The beams at first displace rigidly with the shuttle until they encounter contact pads anchored near their free tips. As each beam breaks, the end displacement is determined from a video image of the structure. Nonlinear beam theory (because of the large deflection), including the compliance of the beam support, is then used to calculate the state of strain in the beam as a function of its tip deflection.

2.3. Bulge specimen testing

The bulge test is one of the first techniques developed for the study of thin films. Beams *et al.* [29] developed the test in 1959. In this method, pressure is applied to a thin film and the deflection is measured as a function of pressure. Using equations relating pressure to deflection, the elastic modulus and residual stress can be computed. In addition, the bulge test can be used to compute the fracture stress and Poisson's ratio for thin film materials. In general, conventional bulge test specimens are circular membranes. However, rectangular and square geometry have also been tested extensively.

Beams [29], assuming that a circular pressurized thin film would take the shape of a spherical cap, derived an expression relating pressure to deflection. Small *et al.* [30] derived a similar expression basing their technique on energy minimization, while Pan *et al.* [31] used FEA to further analyze and verify the test set up.

According to Mitchell [32], fabrication of circular geometries onto a silicon substrate using bulk micromachining techniques is expensive and hard to accomplish. On the other hand, a square suspended film can be easily fabricated using an anisotrpoic etchant such as KOH by micromachining a cavity into the substrate. Several investigators have modeled the behavior of square films subjected to uniform pressure. Timoshenko [33] provided such analysis for deflecting membranes, but his plots do not provide solutions for diaphragms with very large aspect ratios needed to analyze MEMS membranes. Allen *et al.* [34], using energy minimization technique derived a model describing the relation between pressure and deflection for square membranes. Subsequently, Pan *et al.* [31], using FEA, provided a correction to Allen's model. Other investigators, such as Vlassak, *et al.* [35] and Maier-Schneider *et al.* [36] corroborated Pan's analysis.

Other tests exist for characterizing other mechanical properties, such as the elastic modulus, fracture toughness, and hardness for microspecimens. The resonance frequency method can be applied to compute the elastic modulus. Dynamic methods such as the vibrating membrane technique [37] and the vibrating cantilever technique [38] have been applied to evaluate the elastic modulus of thin films. To characterize the hardness and fracture toughness of thin films, the nanoindentation technique [39, 40] is used. Finally, the wafer curvature technique [41, 42] is one of the simplest and most widely used test procedures for determining the residual stresses in thin films.

3. Mechanical behavior of polysilicon

Polysilicon is used in fabricating semiconductor and thin MEMS devices, and it is the most widely used material for such applications. The microstructure of polysilicon depends on deposition conditions [1, 20, 43–47]. When chemical vapor deposition takes place below about 580°C, the deposited polysilicon films are amorphous while above 580°C the films are polycrystalline. These films display fine grain structure if deposited above 600°C, and well defined columnar grain structure perpendicular to the plane of the film if deposited above 625°C. Grain orientation is predominantly {110} when films are deposited between 600–650°C, while displaying {100} orientation when deposited between 650 and 700°C. Doping, oxidation, and high temperatures can cause the grains to grow which leads to increased surface roughness. The polysilicon grains generally have a grain size distribution in the order of 0.2 to 0.5 microns.

Currently, polysilicon is the most widely used material for MEMS fabrication. Several reasons exist for this utilization [18]:

1. Processing of polysilicon is fully compatible with standard IC fabrication techniques.
2. Residual and gradient stresses can be reduced to near zero.
3. Multiple layers of silicon can be deposited and bonded, allowing for fabrication of complex parts.
4. Chemical vapor deposition of polysilicon allows for high conformity, and uniform coating.
5. Polysilicon possesses excellent mechanical properties such as resistance to creep and slow crack growth.

3.1. Polysilicon strength and Weibull effect

The objective of this section is to survey the literature for evidence of a Weibull effect in polysilicon films. Furthermore, whether or not the elastic modulus, E, displays any size dependence will also be addressed.

Sharpe *et al.* [16, 48–50] developed tensile test techniques capable of measuring the mechanical properties (Young's modulus, strength and Poisson's ratio) for thin-film materials. In reference [16], Sharpe *et al.* tested tensile polysilicon specimens with various sizes to determine whether the microstructure, elastic modulus, and fracture strength of these MEMS specimens display size dependence. All specimens were from the same run and had thicknesses of 1.5, 2.0, and 3.5 μm. These tensile specimens were 6, 20, and 600 μm wide, and 250, 1000, and 4000 μm long. Sharpe found that the elastic modulus (as expected) and the microstructure displayed no size dependence. The elastic modulus [50] remained constant (see Table I) even when four different polysilicons from three different suppliers were tested.

However, The strength did display significant strength scatter and size dependence [16]. Since several specimen sizes, with only few specimens per configuration were tested in [16], we have conducted a pooled Weibull analysis on the data to extract the material's Weibull parameters. Pooled Weibull analysis combines all specimen strength data, taking into account the size and geometry difference among tested specimens, and computes a single set of Weibull parameters for that material (the Weibull modulus, m, and the scale parameter, σ_0). The advantage of this method is that by combining all the strength data into one large data set, we obtain a more accurate statistical estimate for the material's Weibull parameters.

In Sharpe's tensile strength data, thick specimens refer to the 3.5 μm thick specimens, while thin refer to both the 1.5 and 2 μm specimens. Narrow specimens refer to both the 6 and 20 μm wide specimens, while wide refer to the 600 μm wide specimens. Based on the data and fabrication process [16], there is a clear difference between the thin and thick specimens as far as strength is concerned. Hence, they are statistically different and should be treated separately. Table II lists the various tensile specimen dimensions and the corresponding number of specimens tested. Pooled Weibull analysis yielded a Weibull modulus $m = 9.4$ for the thin specimens (eight different specimen sizes), and an $m = 30.6$ for all thick specimens (five different specimen sizes). The pooled scale parameters were 4.6 GPa·μm$^{3/m}$ for the thin narrow specimens and 2.1 GPa·μm$^{3/m}$ for the thick specimens.

Assuming that experimental error is at reasonable levels, the large scatter measured in the strength data for polysilicon requires that a probabilistic treatment be used. Since Weibull statistics have traditionally been used to describe strength in bulk ceramics, the question then becomes, is there a size effect in these MEMS tensile specimens? And can we predict that effect using Weibull statistics in a manner similar to bulk ceramics? To begin addressing these questions we'll examine the evidence beginning with [16]. From the data in [16] the thin and thick specimens are treated separately. As stated above there are eight thin narrow specimen sets (with number of specimens tested ranging between 2 and 7 per set). The characteristic strength for each data set (not withstanding the small number of specimens tested for each) was determined individually. The characteristic strength, σ_θ, is defined to be the stress at which 63.2% of the specimens fail. These measured values are plotted in Fig. 4 as a function of the corresponding specimen volume. Also plotted in that figure is a curve fitting the predicted characteristic strengths for all thin specimen sizes, using the characteristic strength of the $2 \times 20 \times 1000$ μm specimen and the pooled Weibull modulus. If a size effect obeying the Weibull theory exists, then we should be able to predict the strength of a given specimen, σ_1, having effective area A_{e1}or volume V_{e1}, knowing the strength of another specimen, σ_2, having effective area A_{e2} or volume V_{e2}, using the following equations,

$$\frac{\sigma_1}{\sigma_2} = \left(\frac{A_{e2}}{A_{e1}}\right)^{1/m} \quad \text{or} \quad \frac{\sigma_1}{\sigma_2} = \left(\frac{V_{e2}}{V_{e1}}\right)^{1/m} \qquad (4)$$

The effective area or volume for a given component is defined to be equal to the area or volume of a tensile specimen subjected to uniform axial tensile stress equal to the maximum effective stress in that component. In a complex structure, the effective stress depends on the multiaxial stress state, fracture criterion, and flaw shape. In a uniaxial uniform tensile stress state, the effective stress is equal to the applied tensile stress. Results indicate that Equation 4 yielded predicted characteristic strengths within 7% of the measured values for five of the seven specimen configurations tested. Note that the eighth data set ($2 \times 20 \times 1000$ μm specimen) is not used to assess the accuracy of the prediction model since that data is used to calibrate or normalize the curve relative to the other specimen sizes (see right most data points in Fig. 4). The two specimen strengths that were not predicted satisfactorily had only 3 data points each and hence larger uncertainty as to the true value of the characteristic strength exists. Please note that for the specimen $1.5 \times 20 \times 1000$ μm, the mean strength was used since Weibull parameters could not

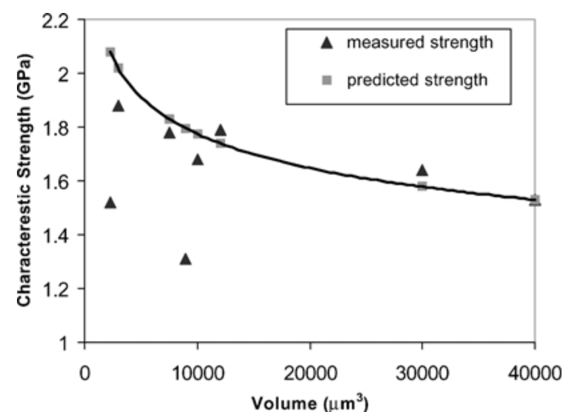

Figure 4 Measured and predicted characteristic strengths as a function of specimen size (volume) for narrow and thin tensile polysilicon specimens.

TABLE I Mechanical properties of polysilicon

Reference/ date	Test	Elastic modulus (Gpa)	Average strength (Gpa)	Weibull modulus	Comments
Sharpe *et al.* [16]/01	Tension	158 ± 10	1.52 ± 0.26[a]	9.4[b]	Strength is mildly dependent on specimen surface area and volume. Microstructure and E are independent of specimen size.
				30.6[c]	
Sharpe *et al.* [50]/00	Tension	158 ± 8	1.56 ± 0.25		Fabricated at Cronos
		157 ± 6.5	3.09 ± 0.18		Fabricated at Sandia National Lab
		164 ± 11.2	2.08 ± 0.35		Fabricated at Standard MEMS Inc.
		152 ± 10	2.00 ± 0.25		Fabricated at Standard MEMS Inc.
Tsuchiya *et al.* [11]/98	Tension	163	2.0–2.8	5.3–6.9	Non-doped. Shown is strength and m range for various specimen sizes. Strength is size dependent (length/side area).
		167	2.0–2.7	8.7–12.6	P-doped. Shown is strength and m range for various specimen sizes. Strength is size dependent (length/side area).
Ding *et al.* [23]/01	Tension	164 ± 1.2	1.24–1.53	10.4–11.7	Shown is strength and m range for various specimen sizes. Strength is size dependent (surface area).
Jones *et al.* [28]/01	Cantilever beam	136[d]	2.7[e] 2%[f]	9.5–14.3	Specimen size variation was very small. Hence, no size dependence was detected.
Greek *et al.* [21]/97	Tension	—	0.77	7	36 thick specimens (10 μm) tested.
			0.57	11	21 thin specimens (2 μm) tested.
Greek *et al.* [20]/99	Tension	162.7[g] 160–167[h]	1.25, 1.19, 1.08, 1.08	10.6, 11.7, 6.1, 11.5	The four strengths and Weibull moduli correspond to the 4 processing techniques. The specimens were 1000 μm long and 10.5 μm thick.
Schweitz *et al.* [72]/99	Tension	172 ± 7	1.76	3	Specimen dimensions are 250 and 1000 μm long, and $10 \times 10\ \mu m^2$ cross section.
LaVan, Tsuchiya, and Coles [12]/01	Tension		4.27 ± 0.61	8.4[i]	98 specimens tested by LaVan.
			3.23 ± 0.25	15.5[i]	19 specimens tested by Tsuchiya.
			2.85 ± 0.40	7.7[i]	28 specimens tested by Coles.
Glass *et al.* [18]/00	Tension	170	2.2 ± 0.4	7.2	48 first generation specimens ($L = 15\ \mu$m and 25 μm, $w = 2\ \mu$m, $t = 2.5\ \mu$m)
			4.3 ± 0.6	8.4	98 second generation conventionally released specimens ($L =$ range between 15 and 1000 mm, $w = 2\ \mu$m, $t = 2.5\ \mu$m)
			2.7 ± 0.6	5.0	50 second generation tungsten coated specimens ($L =$ range between 15 and 1000 mm, $w = 2\ \mu$m, $t = 2.5\ \mu$m)
Bagdahn *et al.* [54]/02	Tension		1.54	11.8	20 μm wide straight tension
			1.27	10.1	50 μm wide straight tension
			2.69	7.5	20 μm wide hole tension
			2.67	8.5	50 μm wide hole tension
			2.83	9.6	20 μm wide notch tension
			2.48	6.2	50 μm wide notch tension
Koskinen *et al.*, [53]/93	Tension of fibers	176 ± 25	2.86 ± 0.28		Average grain diameter = 50 nm
		164 ± 25	2.69 ± 0.30		Average grain diameter = 100 nm
		164 ± 25	3.37 ± 0.29		Average grain diameter = 500 nm
Marxer *et al.*, [56]/97	Tension		3.89 ± 0.53	7.5	Length = 200 μm, width = 2.8 μm.
Ballarini *et al.*, [58]/98	Notched cantilever beam		4.1 ± 0.5	10.8[j]	B-Doped
			4.9 ± 0.4	13.0[j]	Undoped

[a] Average strength of 54 specimens with varying sizes tested in tension. Fabricated at Cronos.
[b] Pooled m for thin specimens as computed by the authors of this paper (see text for explanation).
[c] Pooled m for thick specimens as computed by the authors of this paper (see text for explanation).
[d] E was measured using tensile specimens in a previous round robin study [23].
[e] Strength is obtained by multiplying E by the fracture strain.
[f] Mean fracture strain.
[g] Based on theoretical analysis using elastic compliance constants.
[h] Range of mean E for all four processing techniques obtained experimentally using tensile testing.
[i] Weibull modulus computed using all tested specimens regardless of size, without the benefit of pooled Weibull analysis.
[j] Computed by the authors.

TABLE II Dimensions and number of tensile specimens tested [16]

	6 μm wide 250 μm long	6 μm wide 1 mm long	20 μm wide 250 μm long	20 μm wide 1 mm long	600 μm wide 4 mm long
1.5 μm thick	3	3	4	2	
2 μm thick	7	7	6	5	
3.5 μm thick	2	4	2	2	7

be estimated for a data set with only 2 data points using the maximum likelihood method.

Even better results, as far as size effect is concerned, were predicted for the thick specimens. The Weibull parameters, m and σ_0, for the pooled narrow thick specimens and the individual wide thick specimens were compared. The scale parameters for the two sets are equivalent (2.8 and 2.9 GPa$\cdot\mu m^{3/m}$), while the Weibull moduli are statistically equivalent within a 95% confidence interval. These findings tend to bolster the argument that a size effect exists and can be modeled using the Weibull theory. When similar Weibull analysis based on surface area rather than volume was conducted, similar results were obtained.

Tsuchiya *et al.* [11] tested tensile polysilicon specimens using an electrostatic-force grip technique. The test rig was constructed within a scanning electron microscope (SEM) for *in situ* observation. Tensile specimens with varying sizes were tested in order to statistically study the strength, reliability, size effect, and fracture behavior (location of failure). Non-doped and doped specimens having widths of 2 and 5 microns, and lengths of 30, 100, and 300 microns were tested. All specimens had a thickness of 2 microns. Weibull statistical analysis performed on all 12 data sets yielded Weibull moduli ranging between 5.3 and 6.9 for the non-doped specimens, and 8.7 to 12.6 for the P-doped ones. Low m indicates high degree of scatter in the strength data, and vice versa. In addition, the strength data displayed size dependence, where the strength decreased as the size of the specimen increased. Tsuchiya *et al.* [11] found that the strength depended on the length of the specimen, indicating that these specimens failed due to edge flaws. This prediction was confirmed by the SEM fractographic examination of the fracture surfaces of these thin tensile films. The specimens had many small pits on the surface and notches at the upper corner, remnant from the fabrication process, which caused fracture to initiate at these locations. Tsuchiya correlated his results using the Weibull distribution with very good agreement.

Ding *et al.* [23, 51] conducted similar tensile testing of MEMS polysilicon tensile specimens with varying sizes using a microtensile test device with magnetic-solenoid force actuator. The lengths of the specimens were 660, 300, and 100 μm. The widths of the specimens were 200, 100, 80, 40, and 20 μm. All specimens were 2.4 μm thick. Again, Ding *et al.* found the elastic modulus to be independent of specimen size, while the strength displayed significant scatter and size dependence. Unlike the specimens tested by Tsuchiya *et al.* where size dependence was primarily due to edge flaws (length dependent), these specimens failed presumably due to surface flaws since strength decreased as both length and width increased.

Jones *et al.* [28] tested MEMS polysilicon cantilever beams with mildly varying sizes. The test fixture had the capability of testing several beams simultaneously, which permits efficient testing of large number of specimens. However, this testing technique does not allow direct determination of the stress at failure. Instead, the strain at failure was measured, from which the corresponding stress at failure was computed. The beams tested were fabricated in two different runs of the Multi-User MEMS Processes (MUMPs). A total of 68 and 84 beams were fabricated for the MUMPs19 and MUMPs21 runs, respectively. The MUMPs19 specimens had width of 2.74 μm, thickness of 1.9 μm, and lengths of 50, 60, and 70 μm. The MUMPs21 beams had widths of 2.83 micrometers, and the same thickness and lengths as the MUMPs19 beams. The Weibull moduli for the six different groups of specimens tested ranged between 9.5 and 14.3, indicating statistical scatter in strength, which warrants probabilistic analysis. Because the range of specimen sizes was small (ratio of small to large volume specimens = 0.71), Jones *et al.* observed no size effect, since such an effect was most likely smaller than the scatter in the data [28].

Greek *et al.* [21] were among the first to apply the Weibull theory to predict the strength and reliability of a complex MEMS structure (three-axis accelerometer) using tensile film data. They tested thick and thin films in tension, having thicknesses of 10 and 2 μm, respectively. The widths and lengths of all specimens were 10 and 1000 μm. The mean strength and Weibull moduli for these specimen configurations are listed in Table I. The testing was performed *in situ* within an SEM using a micromanipulator (specimen pulled with a probe arm) in order to locate the critical defects in the material. Qualitative investigation of the fractured regions showed cross sections with slanted flanks resulting in a cross section that is trapezoidal. Sharpe *et al.* [16] also made the same observation when he tested polysilicon films. Greek *et al.* also conducted TEM studies on the films and found the interior of the films to be free from voids or microcracks. Therefore, they assumed that cracking initiated from surface defects, probably in the dry-etched sides, which showed the highest surface roughness. This is important for reliability prediction since it indicates that surface flaws were responsible for failure, and hence surface rather than volume based Weibull analysis should be conducted to predict the strength and reliability of the accelerometers.

In their example, Greek *et al.* [21] transformed the strength of the tensile specimens to predict the strength of the most critical part of a three-axis accelerometer. To measure lateral acceleration, an accelerometer consists of a seismic mass attached to a frame with four elastic beams. When accelerated, the mass will exert a force on the beams, tending to bend each beam as a cantilever. The force acting on each beam corresponded to 1000 g lateral acceleration. The beam had dimensions of length = 300 μm, width = 4 μm, and thicknesses equal to 2 and 10 μm. The maximum stresses generated in the beams were computed to be 16 MPa, while the predicted mean fracture stresses for the thick and thin beams were predicted using Weibull analysis to be 1007 and 698 MPa, respectively. Unfortunately, no actual strength data for the beams were measured to be compared to the predictions. The question whether such seamless extrapolation of Weibull theory to the microsacle level without any modification

for such things as localized source of failure, preferred grain and crystallographic orientation, and grain size to defect size ratio are yet to be answered.

In another study, Greek *et al.* [20] measured the elastic modulus, strength, and Weibull modulus of thick polysilicon films (10.5 μm) deposited using four different processing schemes of doping and annealing, which are known to influence the residual stress and stress gradient state in polysilicon films [47, 52]. These processing schemes yielded compressive residual stress values ranging between 10 and 115 MPa. Tensile specimens were tested *in situ* within a SEM. The elastic modulus was computed in two ways. First it was calculated theoretically using the elastic compliance constants for polysilicon. By taking into account crystallographic texture of polysilicon (obtained via TEM analysis to determine grain growth orientation and X-ray diffraction to determine the texture), the elastic modulus was computed to be 162.7 GPa. Tensile testing yielded an elastic modulus ranging between 160 and 167 GPa. These results indicated that both theoretical and experimental values for E agree within the margin of error, and that E was independent of the doping and annealing process. On the other hand the mean strengths and Weibull moduli did depend on the doping and annealing techniques used in fabricating the specimens.

As can be observed from Table I, different strength results are obtained by different investigators (generally between 0.6 and 4.9 GPa). Such variations have been explained in terms of microstructural differences, size effects, and release processing [12]. In a recent study conducted by LaVan *et al.* [12], the three investigators in three different labs participated in a cross comparison of direct tensile testing techniques. They attempted to study the effect of testing technique and specimen size on the strength and Weibull modulus of polysilicon. Two tensile testing techniques were used. The first employs an electrostatic force gripping mechanism (used by Tsuchiya and Coles), while the second uses a pull-tab tensile specimen (used by LaVan) [17]. The electrostatically gripped specimens had sizes with lengths ranging between 250 and 1000 μm, widths between 6 and 20 μm, and thickness equal to 2.5 μm (four different sizes tested with surface area ranging between 4250 and 45000 μm^2). The pull-tap specimens were significantly smaller (to test for size effect) having thickness of 2.5 μm, width of 1.8 μm, and lengths ranging from 15 to 1000 μm (surface area ranging between 135 and 9000 μm^2).

The mean strengths obtained by Tsuchiya and Coles, who used similar equipment, were within a standard deviation, while the mean strength obtained by LaVan was significantly higher. With regards to how the Weibull moduli compared, the results are questionable. The moduli were computed by combining all strength data for each investigator, without regard to specimen size. In order to correctly compute the Weibull parameters (m and σ_0, where σ_0 is the characteristic strength normalized to unit area or volume) using strength data of specimens with varying sizes, pooled Weibull analysis must be conducted. Hence, no conclusions regarding the similarities or differences between the three Weibull moduli in reference [12], and reproduced in Table I, can be drawn. In general, results from each lab did not show strong size effect even though specimen sizes varied over roughly three orders of magnitude (for both area and volume). Nevertheless, the short specimen data when used with Equation 4 managed to predict the strength behavior of the longer specimens.

Fig. 5 is a plot summarizing the fracture strengths published in six of the references stated above as a function of total surface area of the tensile specimens.

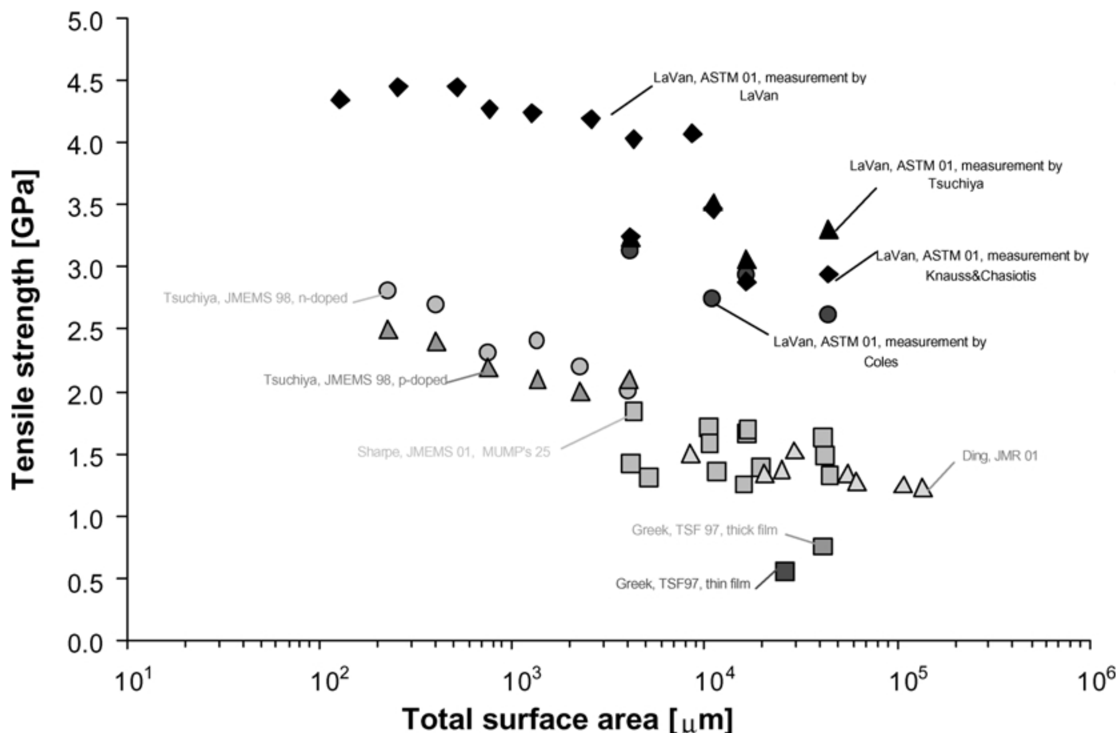

Figure 5 Tensile strength versus the total surface area.

The trend toward decreasing fracture strength with increasing specimen size is reasonably clear in the three different polysilicons of references [10, 11, 16, 23]. The Sandia material of [12] is stronger and shows the same general trend, albeit over a smaller size range. The polysilicon of Greek *et al.* [21] is weaker and shows a reversed trend.

Glass *et al.* [18] conducted extensive testing and fractography using the Sandia pull-tab tensile specimen. In their study, they attempted to characterize the strength distribution, source of failure, and size effect in polysilicon thin film specimens. Two different generations of unnotched pull-tab specimens were tested. The first generation specimens had nominal dimensions of 2 μm wide, 2.5 μm thick, and lengths varying between 15 and 1000 μm to test the effect of gage length on strength. These specimens frequently failed outside the gage length. Therefore, second generation specimens were designed more robustly. Two types of second-generation samples were tested, 98 samples made using two conventional release processes and 50 samples that had post-release coating of tungsten.

The first set of tests conducted by Glass *et al.* [18] was done on a group of 48 first-generation samples, 25 with 25 μm long gage lengths, and 23 with 15 μm long gage lengths. There was no apparent correlation between the strength and the gage length as the 15 μm long samples had an average strength of 2.24 ± 0.37 GPa and the 25 μm long samples had a strength of 2.28 ± 0.39 GPa. The overall average strength for the entire first generation strength was 2.24 ± 0.35 GPa with a Weibull modulus of 7. Similarly, strength results for both the conventionally released and the coated tensile specimens indicated no dependence on size effect even though the length range for these specimens varied over almost two orders of magnitude. Glass *et al.* [18] called this behavior an anomaly, which they are currently studying. They suspect that something in the sample fabrication process caused more severe degradation of the shorter specimens. On the other hand, Glass *et al.* found the tensile strength of amorphous diamond to obey the Weibull size effect because they found the strength to scale with volume [19].

The issue of significant strength scatter for the polysilicon specimens was further discussed by Glass *et al.* [18]. They stated that because the failure origins in their specimens were much smaller (14–44 nm) than the size of the polysilicon grains (<0.5 μm), then the orientation of the grain (which is a silicon single crystal) in which the failure originates could affect the strength. Since strength is a function of fracture toughness, which varies depending on the crystallographic direction, then this variability in toughness will also add to the scatter in strength values.

Koskinen *et al.* [53] investigated the effect of grain size on the strength and elastic modulus of polysilicon (Table I). They performed tensile testing on fibers fabricated from LPCVD films. They found the fibers fabricated with 500 nm grains to be stronger than the fibers made from smaller grains. They attributed that behavior to better interface between the 500 nm grains due to the annealing process.

3.2. Polysilicon strength and Weibull size effect at stress concentrations

Mechanical design of MEMS requires the ability to predict the strength of load-carrying components with stress concentrations. Limited results show that fracture strengths at stress concentrations are larger than would be predicted based on stress concentration factors and material strength. One usually thinks of stress concentrations as weak points in a mechanical structure, and indeed the stress is highest there. However, an increase in fracture stress is observed there in brittle materials because the volume or area of the highly stressed region is smaller. Knowing the variation of the strength with size could be of great benefit to the MEMS community.

Bagdahn, Sharpe, and Jadaan [54] examined the capability of Weibull statistics to predict such localized strengths. Fracture loads were measured for three shapes of polysilicon tensile specimens (1) with uniform cross-section, (2) with a central hole, and (3) with symmetric double notches (Fig. 6). All specimens were 3.5 μm thick with gross widths of either 20 or 50 μm. The holes and notches had radii of 2.5 μm. A total of 226 measurements were made to generate statistically significant information. Local stresses were computed at the stress concentrations, and the fracture stresses there were approximately 90% larger than would be predicted if there were no size effect. Bagdahn *et al.* [54] found that the use of mean strength values without accounting for size effects is inadequate in predicting the load-carrying capacity of components with stress concentrations. For example, the mean strength of 20 μm wide straight specimens was measured to be 1544 MPa. A 20 μm wide hole specimen has a stress concentration factor of 3.23, which means it should break at $1544/3.23 = 478$ MPa. Instead, the average breaking load was 831 MPa—almost a factor of two larger.

This increase in strength was hypothized by Bagdahn *et al.* [54] to be due to the local nature of stresses at the notch roots resulting in reduced effective size and in turn increased strength for the notched specimens. To study the accuracy of this hypothesis, Bagdahn *et al.* [54] used Weibull statistics to determine whether one can predict the fracture strength of the four shapes with stress concentrations from the strengths of straight

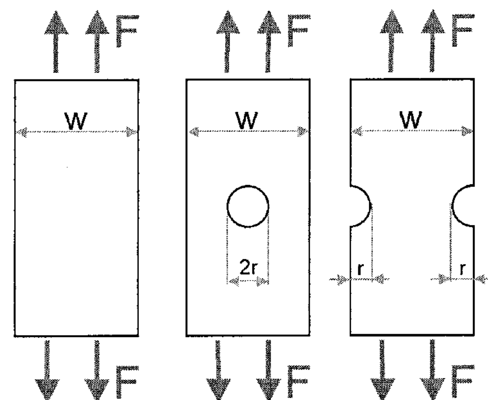

Figure 6 Schematic of the straight, hole, and notch specimens.

specimens. NASA's CARES/Life code [3] and FEA simulation were used to determine the effective volumes and areas of the notched specimens and used these values in Equation 4 to predict their strengths from straight specimens. It was determined that Weibull statistics, taking into account specimen sizes and stress distributions, managed to predict the notched and holed specimen strengths to within ±9% of the fracture strength of the smooth uniaxial tensile specimen configuration. In performing this prediction using Equation 4, Bagdahn *et al.* had to decide what effective size to use. The researchers investigated three effective sizes: the effective volume, effective total surface area, and effective side wall area on the accuracy of the strength prediction. They found the four notched and holed predicted characteristic strengths to be within 51%, 28%, and 9%, respectively of their measured characteristic strengths. These results indicated that proper flaw analysis (volume or surface) based on fractography must be used in order to obtain good strength and failure probability predictions.

Fractography was used by Bagdahn *et al.* to justify the accurate predictions using the side walls as the relevant effective size quantity. Fig. 7 is a montage of typical fracture surfaces at two magnifications in the hole and notch specimens. All of the failed hole and notch specimens showed these features. Some straight specimens had pieces remaining that could be examined in the SEM, and those showed essentially the same features as in Fig. 7. The images in Fig. 7 show that the sidewalls of the specimens are rough with peaks and valleys in the thickness direction that are perpendicular to the loading direction. These will tend to reduce the fracture strength of the material and cause fracture there. This is the reason why using side wall area as the effective size term was the proper choice, which in turn yielded very good predictions. This study clearly supports the hypothesis that the Weibull theory, when properly used, could be extrapolated successfully to predict the reliability and performance of brittle MEMS structures.

3.3. Polysilicon delayed failure due to cyclic fatigue and slow crack growth

Fatigue in ductile materials is generally attributed to plasticity involving dislocation motion leading to crack propagation. On the other hand, fatigue in brittle materials which lack plasticity have been ascribed to degradation in the toughness of material in the wake of the crack tip. According to Muhlstein *et al.* [55], neither of these mechanisms appear to be active in silicon and silicon films at ambient temperatures. While no evidence to date has been presented showing fatigue in bulk silicon,

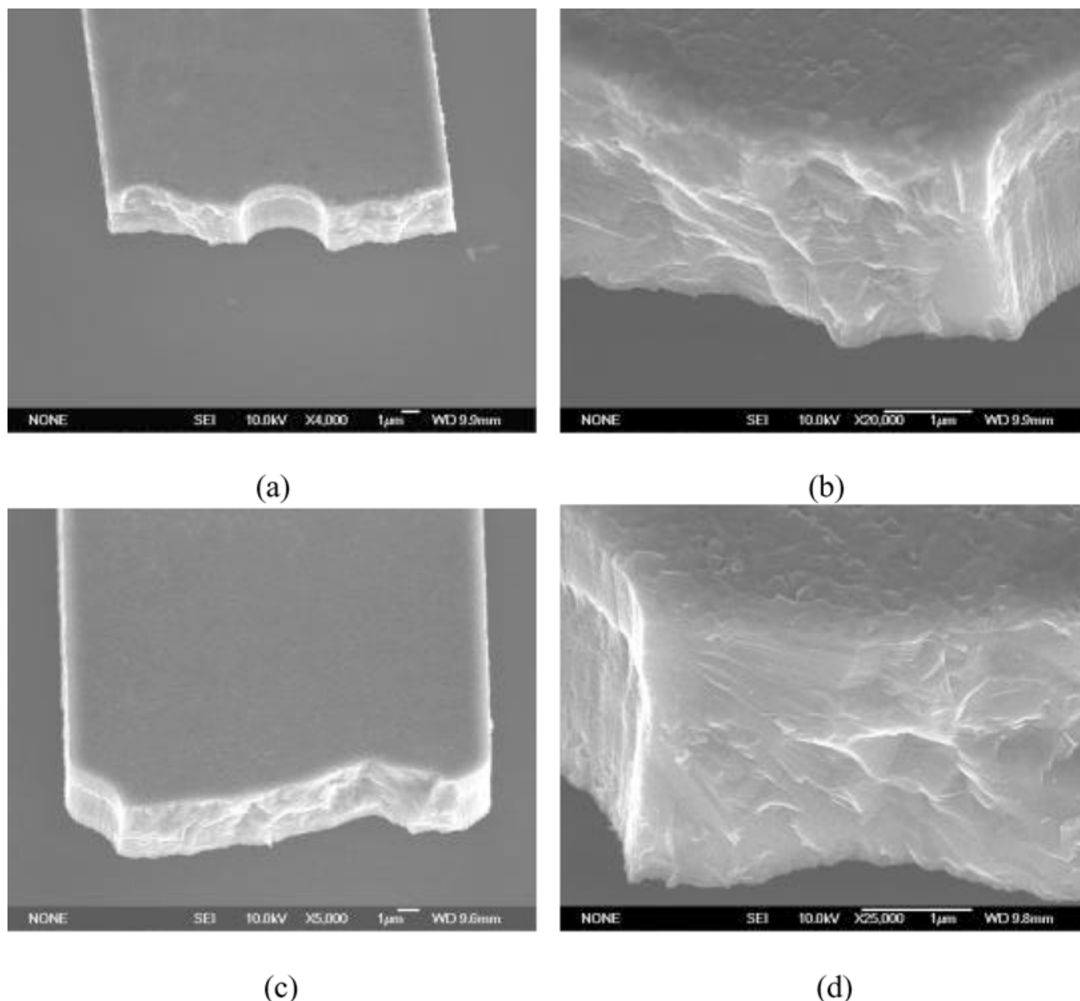

Figure 7 Overview of the fracture surfaces of a hole specimen (a) and a notch specimen (c). Both are 20 μm wide. Magnified views of the locations where failure initiated are shown on the right.

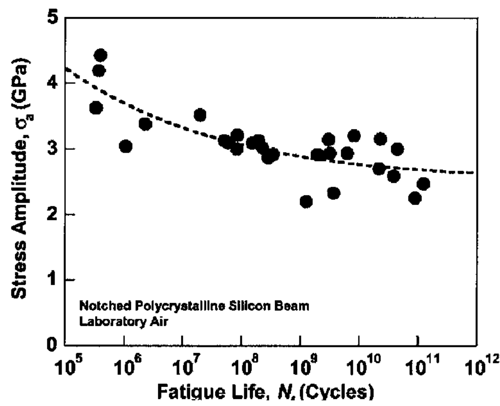

Figure 8 Stress-life (S/N) fatigue behavior of the 2 mm thick, polysilicon at 40 KHz in moist room air under fully reversed, tension-compression loading [55].

fatigue failure in silicon films have been observed repeatedly [55, 56]. Muhlstein *et al.* [55] tested polysilicon notched cantilever beam films and found them to display failure stresses of approximately half their fast fracture strength after fatigue lives in excess of 10^{11} cycles. Fig. 8 obtained from reference [55] shows typical fatigue S-N curve behavior (stress amplitude versus cycles to failure) for 2 μm thick polysilicon films when tested at 40 KHz in moist room air under fully reversed tension compression loading. In that study, the fatigue mechanism was attributed to a process of sequential, mechanically induced oxidation and environmentally assisted cracking of the surface SiO_2 material.

In another study, delayed failure was observed when a REMO (light modulator) in an optical transceiver system failed due to a combination of cyclic fatigue, high voltage, and humidity [57]. The polysilicon actuator included a free-standing membrane that deforms due to electrostatic forces. FEA analysis predicted maximum applied stress of 0.13 GPa due to the applied loading. Fractured tensile specimens (Table I) yielded average strength of 3.89 GPa. As a result, Weibull based fast fracture reliability analysis conducted by Marxer *et al.* predicted essentially no failure. However, after one week of cyclic loading and 80% humidity, the free-standing membrane failed, and the fixed polysilicon electrode delaminated.

In another time-dependent experimental study, Brown *et al.* [56] addressed the issue of environmentally assisted fatigue crack growth in polysilicon. They designed a resonant device containing a notched cantilever beam connected to a wedge shaped mass acting as a resonant mass. By measuring the change in natural frequency (which depends on the stiffness of the structure, which in turn decreases as crack growth occurs) the researchers could detect evidence of crack growth. The tests were performed at 75% relative humidity at room temperature. Plots showing normalized excitation (ratio of excitation to fast fracture excitation) vs. cycles to failure, displayed classic S-N fatigue type behavior. Brown *et al.* argued that crack growth in polysilicon is associated with humidity and attributed it to stress corrosion of the native oxide at the surface of the specimen.

Another group of researchers showed that subcritical crack growth due to fatigue loading can take place with very little (and perhaps no) humidity [58]. Ballarini *et al.* [58] in an attempt to measure the toughness and subcritical crack growth behavior of polysilicon films designed and fabricated a fracture mechanics specimen that was fully integrated with an electrostatic actuator. Their arrangement allowed the entire fracture experiment to take place on-chip without the need for an external loading mechanism. Fracture testing was conducted under fast fracture and cyclic resonance loading. The fracture specimen consisted of a notched cantilever beam attached to a released actuator. FEA was used to determine the stress intensity at the notch tip. Because the notch tip was blunt, hence not representing a sharp crack tip necessary for actual fracture toughness measurement, Ballarini *et al.* reported maximum principal stresses (Table I) and critical J-integral values for fracture.

Kapels, Aigner and Binder [59] developed a novel thermal actuation test arrangement that permits both monotonic loading and tension-tension fatigue testing. The specimen, much smaller than the thermal actuator (5 μm long $\times$ 0.7 μm wide and 4 μm thick), is fastened to the substrate through a large anchor, which also serves as a heat sink to keep the specimen from heating. Cyclic heating of the arms at a rate of 1 Hz pulls the specimen in tension-tension fatigue. Kapels *et al.* found that failure due to fatigue loading in their polysilicon specimens did take place. What is even more remarkable is that these fatigue failures were detected within one million cycles in contrast to the billion or more cycles necessary to induce failure using the resonant test methods.

The fatigue behavior of 3.5 μm thick and 50 μm wide polysilicon tensile specimens (see Fig. 2) under tension-tension cyclic loading was investigated by Bagdahn and Sharpe [60]. It was shown, that the strength of the samples decreased with increasing number of cycles (the tensile strength of 1.1 GPa for virgin samples decreased by about 35% to a fatigue strength of 0.70 GPa after 10^9 cycles). No influence of frequency on the number of cycles to failure in the range of 50 Hz to 6000 Hz was observed by the investigators.

In order to assess the role of SCG in polysilicon, Ballarini *et al.* [58] allowed the notched beams to resonate at subcritical stresses until fracture. Cyclic fatigue results were plotted as S-N curves where S is the maximum tensile stress at the notch root, and N is the number of cycles to fracture. Tests were conducted at room temperature and 40% relative humidity. Significant scatter existed in the data. However, it was apparent that fatigue fracture could occur after as many as 10 billion cycles. Results also indicated that fatigue crack initiation and growth could take place in both air and low pressures (tests conducted in vacuum chamber at 8 MPa), but the process is faster in air because of stress corrosion due to humidity. Van Arsdell [61] was yet another investigator who detected environmentally assisted crack growth in polysilicon MEMS devices.

3.4. Polysilicon fracture toughness

Fracture toughness of polysilicon has not been as extensively investigated as the other mechanical properties.

Jackson *et al.* [62] measured the fracture toughness of polysilicon by introducing various sized corner notches in tensile specimens using a focused ion beam. Specimen gage widths were 1.8 or 3.8 μm, while the notches were 100–500 nm long on a given side. The tensile specimens were subsequently broken using the Sandia National Lab nanomechanical testing system with lateral force capabilities. Using SEM, Jackson *et al.* measured the dimensions of the initial elliptical corner notch and computed the fracture toughness using classical fracture mechanics theory. Two different corner elliptical crack solutions were computed for each test. Specimens survived intact showed fracture surface details, including the initial notch, mirror, and hackle regions. These were used to compute the fracture toughness. As was found by Bagdahn *et al.* [54] and shown in Fig. 7, the fracture surface markings for these MEMS specimens were found to be similar to those observed in bulk ceramics. The long specimens (500 μm and 1000 μm long) shattered at failure and did not survive to show any fracture surface markings. Results of eleven tests yielded average values of 1.58 ± 0.26 MPa$\cdot$m$^{1/2}$ for the elliptical crack analysis and 1.68 MPa$\cdot$m$^{1/2}$ for the modified elliptical crack analysis. Jackson *et al.* stated that these values could be inflated by about 25% since in previous studies the Sandia tensile test yielded 25% higher forces compared to other researchers. At any rate, these values are in the same range as those measured by Sharpe *et al.* [63] of 1.4 MPa$\cdot$m$^{1/2}$, Kahn *et al.* [64] of 1.2 MPa$\cdot$m$^{1/2}$, Ballarini *et al.* [65] of 1.0 MPa$\cdot$m$^{1/2}$, and Bagdahn *et al.* [66] of 0.86 MPa$\cdot$m$^{1/2}$.

In the fracture toughness tests surveyed above except [64–66], the notch roots introduced to the specimens possessed finite dimensions. This is not in conformity with fracture mechanics theory, which assumes the existence of sharp crack tip. More research is needed to develop proper MEMS fracture mechanics specimens if accurate determination of the fracture toughness parameter is to be determined.

3.5. Polysilicon high temperature properties

High temperature testing of MEMS remains a field seldom studied where data is very sparse and hard to come by. If MEMS devices are to be used in high temperature applications, then their mechanical properties at such temperatures must be assessed. This is necessary in order to design more reliable and durable MEMS structures.

Few studies exist where the effect of temperature on the elastic modulus, E, in MEMS was considered [67–69]. Michalicek *et al.* [67] found E of polysilicon to decrease from 163 GPa at room temperature to 158 GPa at 180°C. Kahn *et al.* [68] measured E of an in-plane microstructure heated resistively and found it to decrease from 168 GPa at room temperature to 163 GPa at 450°C. Eby *et al.* [69], using two different tensile specimen configurations (narrow and wide) found E to decay from 160 GPa at room temperature to 149 GPa at 250°C.

Similarly, studies investigating the thermal expansion coefficient (TEC) of polysilicon are rare [69]. Chae *et al.* [70] measured the TEC for polysilicon to be 2.9×10^{-6}/°C, Wong *et al.* (private communication in reference 60) found it to be 4×10^{-6}/°C, while Jensen *et al.* [71] obtained a value of 4.4×10^{-6}/°C. Eby *et al.* [69], measured the TEC to be 4.9×10^{-6}/°C on heating and 4.7×10^{-6}/°C on cooling using narrow tensile specimens tested in free expansion. To check their results, Eby *et al.* tested the wide specimen using another method (applying stress well below fracture, fixing the grip ends, and heating the specimen) and still found the TEC to be 4.7×10^{-6}/°C in cooling. Additionally, Eby *et al.* measured Poisson's ratio as a function of temperature and found it to remain constant at 0.22 between room temperature and 250°C.

To assess the strength of polysilicon as a function of temperature, Eby *et al.* [69] tested 16 narrow specimens and one wide specimen in tension. They showed the strength to remain constant between room temperature and 250°C. Significant scatter in strength values, as expected, were observed.

The findings summarized above, including low Weibull moduli and size dependence, indicate that MEMS polysilicon devices tend to display similar probabilistic behavior to that of bulk monolithic ceramics. Therefore it would be prudent for the design of polysilicon MEMS devices to be based on probabilistic techniques, similar to those used for bulk ceramics, in order to reliably predict their short and long term behavior. It is apparent that the MEMS community has already adopted such approaches as evidenced by their extensive use of Weibull statistics and probabilistic based design to characterize the strength and reliability behavior of MEMS devices.

3.6. Delamination of bonded silicon

Delamination (debonding) is a recurring mode of failure in wafer-bonded MEMS. The fabrication of many silicon micromechanical components, such as acceleration sensors, gyroscopes, micropumps, or microvalves frequently involves joining two or more wafers. Kohler *et al.* [72] studied the mechanical reliability of bonded silicon microsystems. They examined the fracture strength and durability of a bond (interface layer) using burst tests and Weibull statistics. The Weibull failure probability approach for bonded interfaces provides a method allowing differently sized and shaped devices to be compared. They investigated the effect of annealing temperature, length of bond edge (specimen shape), and thermal and cyclic (vibrational) fatigue on the failure probability of bonded interfaces. The interface quality using the Weibull modulus, the mean fracture stress per unit edge length, and the surface energy of the bond was characterized. However, it needs to be pointed out that in this study the stress component used to assess the bond strength between the bonded films was the bending stress at the edge of a clamped plate, as derived by Timoshenko [73], to describe the stress distribution at the bond boundary. Instead, debonding should have been characterized using peel stress (stress normal to bond interface), shear stress, or a combination of the two stress components similar to what was done in reference [74].

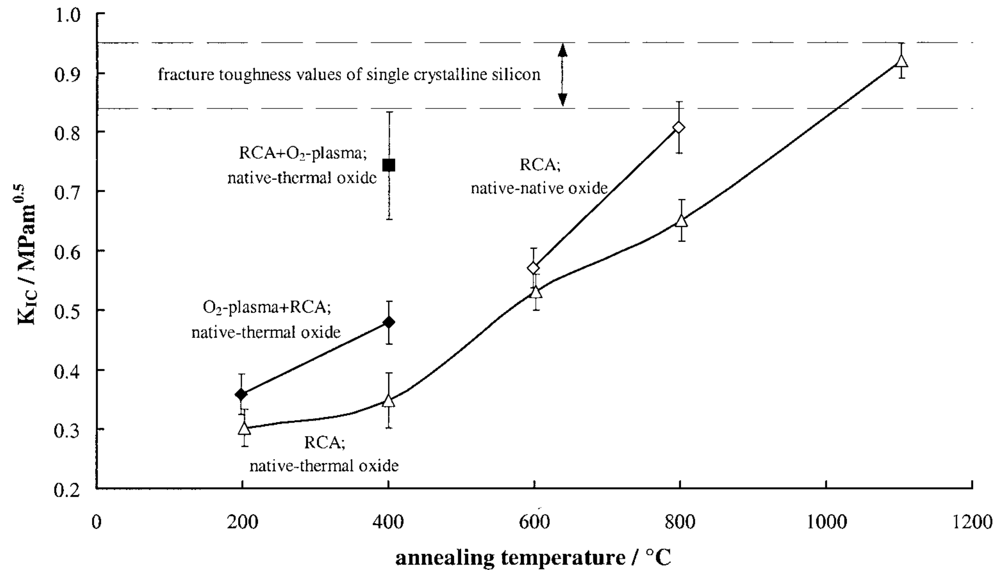

Figure 9 Fracture toughness (average values and standard deviations derived from 52 measurements) as a function of the wafer bonding conditions and annealing temperatures. The lower and upper boundary for single crystalline silicon relate to the fracture toughness values of the {111}- and {100}-orientations [76].

In their tests, Kohler *et al.* [72] bonded two 100 mm diameter silicon wafers having 525 μm thickness each. These bonded pairs had a cavity in one wafer and a gas inlet in the other. The tests were conducted by applying gas pressure between the bonded wafers. The resulting fracture probabilities were then correlated to annealing temperatures and fatigue loading. In summary the following observations were made: (1) the strength, and hence probability of survival, improved with the increase in annealing temperature; (2) size effect characterized by the decrease in bond strength as the length of bonded edge between the two wafers increased was found. The Weibull theory successfully predicted the failure probability of the differently shaped and sized specimens; and (3) the bond reliability (strength and survival probability) degraded with both thermal cycling and vibration. This is yet another MEMS failure mode where crack growth and delayed failure should be accounted for.

A method for measuring the fracture toughness of wafer-bonded silicon was developed by Bagdahn *et al.* [75] and Petzold *et al.* [76]. Their approach is based on the well known Chevron test. The advantages of the test are the self initiation of a sharp pre-crack during the first stage of the test and that no crack length measurement is necessary for the determination of the fracture toughness. Since, the fabrication of the required chevron structure can be integrated into the normal fabrication flow of wafer-bonded devices the samples can be easily produced and no additional preparation like sawing is required before testing. It was shown by these investigators that the fracture toughness strongly depended on the pre-treatment of the surfaces before bonding and the annealing temperature (Fig. 9).

Fatigue investigations of directly bonded silicon have been performed by Bagdahn and Petzold [77]. They found slow crack propagation to take place using a modified double cantilever beam test in the bonded interface. The slow crack growth is caused by stress corrosion of siloxane bonds in the wafer-bonded interface. It was shown that the crack growth rate depended on the bonding parameter and the environmental conditions during testing (water increases the crack growth rate). Delayed failure was observed under both static as well as cyclic long-term loading. Further investigations by the same authors [78] revealed that delayed failure under static and cyclic loading (up to 40 Hz) is solely controlled by stress corrosion in the bonded interface. Therefore, life under cyclic loading depends on the frequency (Fig. 10) but can be predicted based on results from static crack growth measurements using the approach by Evans and Fuller [79].

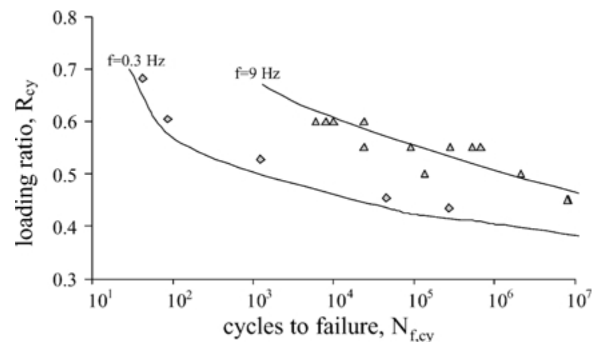

Figure 10 Loading ratio (average load/maximum load during cycling) for two different frequencies versus the cycles-to-failure (symbols: experimental results, lines: predictions) of directly bonded silicon [78].

4. Mechanical behavior of single crystal silicon

Single crystal silicon (SCS) material has a cubic crystal structure and can be fabricated with very low lattice defect densities. Silicon used for semi-conductor applications is fabricated using the Czochralski growth or the floating zone methods with either p- or n-doping [81]. Wafers with $\langle 100 \rangle$ and $\langle 111 \rangle$ crystal orientations are most commonly used in the IC industry, while for MEMS fabrication the $\langle 110 \rangle$ wafers are often used as well.

An important question regarding single crystal failure behavior is what determines the crystallographic planes on which cleavage occurs? Shultz *et al.* [82] wrote a review paper addressing that question. One theory considered a correlation between preferential cleavage planes and *crystal growth planes*. For example, such correspondence exists for halite (NaCl) structure on the {100} planes, and the {111} planes for the fluorite (CaF2) structure. However, this correspondence between the cleavage and crystal growth planes was not found to be true for most other crystals and hence judged not to be a valid criterion for cleavage. Two other ideas attempting to provide cleavage criteria were based on the concepts that cleavage planes coincide with *planes that bound a unit cell* and the *most closely packed crystal planes*. Again these criteria were found to be valid for some crystal structures but failed once applied to wider range of crystals. Hence these concepts were also rejected as universal ideas for cleavage planes. The three theories just stated are based on correlating the cleavage planes to the crystal structure.

Failure of the approaches stated above led to the conclusion that it is the properties of the crystal structure rather than the crystal structure itself that should be examined. Various crystal properties were examined as possible cleavage criteria [82]. These concepts are built on the notion that cleavage constitutes braking of bonds between atoms and ions. Some of these theories are:

- The bond density concept: states that the minimum number of bonds per unit area determines the cleavage plane.
- The elastic modulus concept: since the elastic modulus is one physical property directly associated with strength of bonds, it was also considered as cleavage criteria. Stronger bonds should result in higher elastic modulus perpendicular to the crystal plane, and vice versa.
- The surface energy concept: states that the cleavage plane is the plane of minimum surface energy.

The crystal properties based theories listed above suffer from the same problem as the crystal structure based concepts. Namely, they are not universal and sometimes they fail to predict the cleavage planes for the simplest cases. Shultz *et al.* [82] state that this outcome should not be surprising given that the cleavage process is dynamic in nature, while all concepts listed above are based on static or quasi-static approaches. Therefore, if a cleavage criterion is to be applicable it should be dynamic in nature. In addition, theoretical approaches to predicting the cleavage planes proved fruitless, indicating that these planes are to be determined experimentally using a measured material parameter.

Fracture toughness (K_{Ic}) of the crystallographic planes [82] (cleavage toughness) proved to be the most appropriate criterion. Based on experimental data, the cleavage plane was found to coincide with the crystallographic plane having minimum K_{Ic} for ionic and covalently bonded structures. For example, the fracture toughnesses for single crystal silicon on the {100}, {110}, and {111} planes were measured to be 0.95, 0.9, and 0.82, respectively [83]. Accordingly, the well-established cleavage plane {111} had the lowest K_{Ic}. These measurements and predicted cleavage plane concept were consistent with the experimental strength determinations of Wilson and Beck [24]. They examined the strength of silicon cantilever beams and found significant variation in strength and dependence on orientation. The strengths were found to be 3 GPa and 1 GPa when fracture occurred on {110} and {111} planes, respectively.

Stress calculation requires knowledge of the elastic constants. For homogeneous isotropic materials these parameters (E, ν) remain constant and do not vary with orientation. However, for crystals these parameters vary with orientation within a specific crystallographic plane. Generalized equations describing how the elastic modulus [84] and Poisson's ratio [85] change with orientation have been derived and numerically evaluated for all possible directions within the important {111}, {100}, and {110} planes. Brantly [85] showed that for cubic crystals, elastic isotropic conditions (E and ν remain constant) exist for all directions within the {111} plane. This is a significant finding, since fracture in single crystal silicon is often associated with {111} plane, which is the lowest fracture energy cleavage plane for silicon, as will be discussed later. Hence for fracture stress analysis, it is reasonable to use isotropic properties as long as failure is associated with the {111} plane. K.-S. Chen *et al.* [86] conducted FEA analysis on silicon biaxial flexure disks. They performed two types of analyses: (1) elastically isotropic two dimensional (axisymmetric) analysis, and (2) crystallographic cubic three dimensional analysis. They determined that the stress solutions, including peak stresses, for the two solutions are always within 3%. Brantley [85] also showed that the ratio $E/(1-\nu)$, known as the biaxial modulus, is invariant for all directions within the {100} planes, while for the {110} planes E, ν, and the $E/(1-\nu)$ vary with orientation. He computed E to be 168.9 GPa for all directions within the {111} plane, 168.9 GPa and 130.2 GPa within the {100} plane in the ⟨110⟩ and ⟨100⟩ directions respectively, and 187.5 GPa and 130.2 GPa within the {110} planes in the ⟨111⟩ and ⟨100⟩ directions respectively.

Tsakalakos [87] conducted theoretical and experimental studies on the deformation of membranes in the biaxial bulge test. The bulge test is one of the first techniques developed for the study of thin films. Using this method, pressure is applied to a thin film that has been clamped over a circular or square opening. Tsakalakos derived expressions for the biaxial elastic modulus $Y[hkl](Y = E/(1-\nu)$ for isotropic materials) for the {100}, {110}, and {111} crystallographic orientations in the plane of cubic crystal membranes. The biaxial elastic modulus, Y, relates the stress, s, and strain, e, at the center of the bulged diaphragm according to $s = Y[hkl]e$. Y is measured, and subsequently compared to the theoretical solution, for a given crystallographic direction in the plane of the film using the slope of the stress-strain curve of a bulge test.

TABLE III Weibull parameters for the bend specimens tested bay Namazu *et al.* [91].

	Specimen	Upper width w_1 (μm)	Lower width w_2 (μm)	Thickness t (μm)	Length l (μm)	Tip radius R (μm)
Nanometer scale	A	0.2	0.37	0.255	6	<0.1
	B	0.3	0.47	0.255	6	
	C	0.8	0.98	0.255	6	
Micrometer scale	D	4.75	7.5	1.91	35	1
	E	48	74.5	19	360	10
Millimiter scale	F	1045	1800	520	9850	200

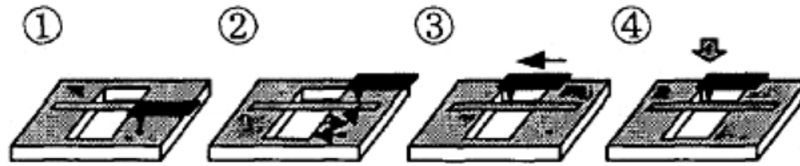

Figure 11 Schematic diagram of bend test specimen [91].

4.1. SCS strength

Significant scatter in strength have been demonstrated experimentally for SCS material. Hu [88] tested silicon wafers with {100} and {111} orientations. The specimen configuration Hu tested consisted basically of a 5 mm diameter simply supported wafer pushed against with a concentrated load (via a spherical ball) applied at the center of the disk. Table III contains a summary of Hu's strength data. These results showed two main points: (1) significant scatter in strength data exist, as demonstrated by the standard deviations for both crystallographic orientations, and (2) consistent with what was stated earlier, wafers with {111} orientation exhibited lower strength than the {100} wafers, albeit not being statistically significant due to the large standard deviations for both sets of data.

Early investigators had observed size effect in SCS. They showed that silicon whiskers with small cross sections exhibited higher strengths than ones with larger cross sections. For example, Eisner [89] measured the strength of 1 μm diameter whiskers to be 3.5 GPa, while for whiskers with 20 μm diameter Pearson *et al.* [90] found the average strength to be 2.2 GPa.

One of the most significant studies regarding the size effect on strength and probabilistic behavior of SCS material was conducted by Namazu *et al.* [91]. In that study, the investigators tested the strength and elastic moduli of nanometer, micrometer, and millimeter scale SCS bend specimens. The centrically loaded double edge fixed beams (see Fig. 11) were oriented along the ⟨110⟩ direction in the {100} plane. The beam dimensions are listed in Table III, which was obtained from Namazu *et al.* [91]. Results indicated that the SCS elastic modulus was independent of size (169 Gpa), while the bending strength displayed significant sensitivity to size. Fig. 12 shows the Weibull strength distributions for the various beam configurations tested by Namazu *et al.* As can be seen from the plot, the bending strength increased as the size decreased from millimeter to nanometer scale dimensions. Namazu *et al.* [91] stated that the average bending strength for the nanometer scale beam with a width of 200 nm was found to be 17.5 GPa, which was 2.3 to 4.7 times greater than the bending strength of the microsized beams, and 38 times greater than that for the millisized beams. They also observed a reduction in the Weibull modulus (strength scatter increased) as specimen sizes increased.

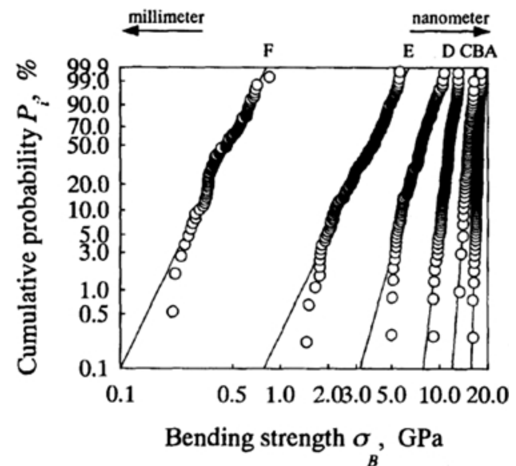

Figure 12 Weibull plots of bending strength distributions for the nano, micro, and millimeter specimens [91].

Wilson *et al.* [25] characterized the strength of SCS by fracturing microcantilever beams etched into {100} silicon wafers. Front sides (top surface of beam) were etched using reactive ion etching (RIE), which produced smooth surfaces, while for the back sides (bottom surface), anisotropic etching (KOH) was used yielding rough surfaces. The beams were oriented so their lengths were along the ⟨110⟩ direction. The beam dimensions are listed in Table IV. FEA was used to compute the fracture stresses for the tested beams. This was necessary in order to account for large beam deflections, material anisotropy, and the nonideal support where the beam joins the wafer. At the support, a 54.7° angle between the beam oriented along the {100} crystalline plane and the {111} plane in the base of the wafer was present. This geometry caused the stress at the fixed end due to front loading (force pushing down) to be lower than the stress due to back loading (force pushing up). Since the axial direction of the beam was along the ⟨110⟩ direction, the lateral in-plane direction of the beam was also along the ⟨110⟩ direction. The axis orthogonal to the plane of the beam was along the ⟨100⟩

TABLE IV Strength for SCS material

Reference/year	Specimen	Average strength (GPa)	Wafer orientation/ specimen direction	Weibull modulus	Comments
Hu [88]/82	Flexural plate	2.1 ± 0.8	{111}		Simply supported circular wafer with 5 mm diameter.
		3.0 ± 0.87	{100}		
Namazu *et al.* [91]/00	Beam	17.5	{100}/⟨1110⟩	62	Nano-beam A (see Table III & Fig. 12)
		15.3		26.6	Nano-beam B (see Table III & Fig. 12)
		11.6		16.8	Nano-beam C (see Table III & Fig. 12)
		7.7		7.2	Micro-beam D (see Table III & Fig. 12)
		3.7		4.2	Micro-beam E (see Table III & Fig. 12)
		0.5		4.2	Milli-beam F (see Table III & Fig. 12)
Wilson *et al.* [25]/95	Cantilever beam	3.6 ± 0.7	{100}/⟨011⟩[a]		Front side of wafer (smooth surface). Dimensions: 350–750 × 200 × 16–30 μm.[b]
		1.1 ± 0.2	{100}/⟨011⟩		Back side of wafer (rough surface). Dimensions: 350–750 × 200 × 16–30 μm.
Wilson and Beck [24]/96	Cantilever beam	1.3 ± 0.3	{100}/⟨011⟩		Fracture surface along {111} plane. 103 specimens failed accordingly.
		2.3 ± 0.4	{100}/⟨011⟩		Fracture surface along {011} plane. 80 specimens failed accordingly.
Johansson *et al.* [26]/88	Cantilever beam	3.9	{100}/⟨011⟩		Majority of beams fractured in the 3–4.9 GPa range.
		4.3	{100}/⟨001⟩		Majority of beams fractured in the 0–6 GPa range.
Ericson *et al.* [27]/90	Cantilever beam	6.1 ± 0.8	{100}/⟨001⟩	10.1	Reference untreated specimens
		4.1 ± 0.8		6.3	Polished (0.25 μm) specimens
		7.2 ± 0.4		32.3	Polished and oxidized specimens
		6.6 ± 0.9		8.1	Polished, oxidized and then stripped
Ando *et al.* [22]/00	Tension	4.1 ± 0.9	⟨011⟩	3.6[c]	Specimen dimensions: 50 × 50 × 5 μm.
Yi *et al.* [93]/00	Tension	0.63 ± 0.07	⟨011⟩	13.4	Specimen etched using KOH
		1.24 ± 0.3		5.4	Specimen etched using EDP
		0.83 ± 0.3		3.6	Specimen etched using TMAH
		1.01 ± 0.5		2.6	Specimen etched using XeF2
Schweitz *et al.* [80]/99	Tension	1.73	⟨001⟩	5	Specimen dimensions are 250 and 1000 μm long, and 10 × 10 μm^2 cross section.
K.-S. Chen *et al.* [86]/00	Biaxial flexure	1.2[d]	{100}	2.7	Mechanically ground (A)
		2.3[d]		3.4–4.2	Mechanically ground (B)
		3.4[d]		7.2–12	KOH-etched
		4.6[d]		3.3	STS DRIE
C. Chen *et al.* [95]/85	Biaxial flexure	0.31	{100}	4.5	Circular wafers with diameter = 50 mm, thickness = 0.33 mm.

[a] {ijk} refers to type of Si wafer, while ⟨ijk⟩ refers to crystallographic orientation along the beam.
[b] Beam length varies between 350 and 750 μm, width = 200 μm, and thickness varies between 16 and 30 μm.
[c] Calculated by the authors using graphical strain data from reference [22].
[d] Characteristic strength.

direction. Wilson *et al.* [25] incorporated this material anisotropy in their FEA model by using the appropriate elastic modulus, shear modulus, and Poisson's ratio (see Table V). In Table V, Wilson *et al.* derived $E\ \langle 110\rangle$ by calibrating the analytical FEA model to experimental measurements, while the rest of the material constants were based on theoretical calculations [85]. It is interesting to note the correlation between the experimental $E\ \langle 110\rangle = 161$ GPa as measured by Wilson *et al.* and the corresponding theoretical value of 168.9 GPa as computed by Brantley [85].

The resulting Wilson *et al.* strength data showed significant scatter, consistent with brittle material behavior. The front loaded beams, failing due to defects at the top smooth surfaces, yielded strengths varying between 0.7 and 5 GPa, while the back loaded beams, failing due to defects at the back rough surface, yielded strengths varying between 0.7 and 1.5 GPa.

Fracture surface analysis performed on the beams indicated that distinct differences in the surfaces existed when beams fractured at the top surfaces as opposed to the bottom. One expects that cleavage would take place along the {111} planes having the lowest surface energy. However, the loading geometry and boundary conditions can cause secondary cleavage planes to be activated [25]. In a subsequent study, Wilson and Beck [24] investigated the issue of preferential fracture planes in SCS. They tested the same microcantilever beams discussed above with the exception that they were side loaded. This was done to investigate the effect of beam side roughness as well as the orientation of initiating fracture planes. Fracture initiated along either {111} or {110} planes and was observed experimentally using SEM. In a few cases, fracture starting along a given plane then shifted into another. Comparison of the fracture types indicated that the {110} strength was greater than that for the {111} plane (Table IV); the difference in strength was attributed to the location of fracture initiation. The {110} fracture, for which the plane is perpendicular to the beam axial direction, initiated in the beam's maximum stress region, while the {111} fracture, which is inclined to the beam's axial direction, initiated at the bottom (back) surface of the beam and then progressed along a {111}

TABLE V SCS elastic properties

Reference	Direction	Elastic modulus (GPa)	Shear modulus (GPa)	Poisson ratio
Brantley [85]/73[a]	⟨100⟩	130		
	⟨110⟩	169		
	⟨111⟩	187.5		
Namazu *et al.* [91]/00	⟨110⟩	169.9[b]		
		167.9[c]		
		169.2[d]		
Wilson *et al.* [25]/96	⟨100⟩	130	50	0.064
	⟨110⟩	161	80	0.279
Sato *et al.* [92] /98[e] and Ando *et al.* [22]/00	⟨100⟩	138 ± 11		
	⟨110⟩	140 ± 25		
	⟨111⟩	180 ± 20		
Yi *et al.* [93]/00	⟨110⟩	169.2 ± 3.5		
Schweitz *et al.* [80]/99	⟨100⟩	142 ± 9		

[a]Based on theortical computations using material's elastic constants.
[b]Measured from force-deflection diagrams of nanometer scale beams.
[c]Measured from force-deflection diagrams of micrometer scale beams.
[d]Measured from force-deflection diagrams of millimeter scale beams.
[e]Values read from bar graphs in reference [92].

plane in a region where smaller stresses are found. It is concluded therefore, that the right combination of stress magnitude and critical defects could cause fracture to take place along secondary strong planes with higher surface energies.

Other investigators have also attempted to characterize the strength of SCS material. Johansson *et al.* [26] tested SCS cantilever beams. The beams had lengths varying between 75 and 500 μm, widths between 75 and 240 μm, and thicknesses from 8 to 16 μm. The beams were fabricated from {100} wafers and oriented along the ⟨100⟩ and ⟨110⟩ directions. The corresponding strength results are listed in Table IV. However, these strength values are not accurate and should not be used to characterize the strength of SCC because Johansson *et al.* used classical mechanics of materials theory for cantilever beams to compute the stresses. This is inaccurate because large deflections (deflection to thickness ratio in the order of two and higher) and material anisotropy exist for these beams. Nevertheless, the following findings can still be considered qualitatively acceptable. First, the strength distribution displays wide scatter behavior. And second, no size effect based on width was detected [26]. It is unfortunate that the authors did not study the size effect on the basis of stressed specimen surface area, volume, or edge length. The lack of size effect as reported by Johansson *et al.* could very well be due to the small variation in tested specimen widths (less than a factor of 4).

Ericson and Schweitz [27] used Weibull statistics to study the effects of processing techniques on the strength of SCS cantilever beams exposed to various surface treatments like diamond polishing, oxidation, and stripping of the oxide layer. The beams were oriented along the ⟨110⟩ direction in the plane of {100} silicon wafer. The beam dimensions were $197 \times 134 \times 17$ μm. Different grades were used to polish the beams (0.25, 1, and 3 μm) and the strength results for the unpolished (reference) beams as well as the 0.25 μm polished beams are listed in Table IV. Diamond polishing was found to degrade the strength significantly. However, polishing followed by oxidation not only restored that strength but actually improved it, possibly due to crack healing. Polishing, oxidation, and subsequently stripping the oxide layer yielded strengths slightly less than the reference values. According to the authors, the elevated strengths in this study compared to others were due to improved processing techniques.

Fast fracture and cyclic fatigue testing was performed on SCS tensile specimens oriented along the ⟨110⟩ crystallographic direction by Ando *et al.* [22]. The straight portion of the film specimens had dimensions of $50 \times 50 \times 5$ μm. Ando *et al.* also measured the elastic modulus along the ⟨110⟩ direction and found it to be 140 ± 25 GPa which is 17% less than that computed by Brantley [85] using elastic constants (169 GPa). The average fracture strain was measured at $3.4 \pm 1.0\%$, which corresponds to an average strength of 4.1 ± 0.9 GPa, indicating large strength scatter for SCS. In a previous study, Sato *et al.* [92] measured the elastic moduli (Table V) and fracture strains for SCS using larger tensile specimens (400 μm long $\times$ 100 μm wide $\times$ 20–30 μm thick) oriented along various crystallographic directions. The ⟨100⟩ and the ⟨110⟩ oriented tensile specimens were fabricated from {100} wafers, while the ⟨111⟩ oriented tensile specimens were fabricated from {110} wafers. These measured elastic moduli are compared to the ⟨110⟩ modulus measured by Wilson *et al.* [25] and the theoretically computed value as described by Brantley [85], and were found to be within reasonable agreement. Sato *et al.* did not report the fracture strengths for the tensile specimens, but rather reported fracture strains. These fracture strains were found to be small (0.4–2.3%) compared to the specimens tested by Ando *et al.* (note that the Sato and the Ando studies are performed by the same investigators), which could be related to size effect.

Yi *et al.* [93] used SCS microtensile specimens oriented along the ⟨110⟩ direction to measure the elastic modulus, and to study the effect of four different etchants (KOH, EDP, TMAH, XeF2) on the strength (Tables IV and V). Their tensile testing technique was similar to that pioneered by Sharpe and described earlier [16, 48, 49]. The specimen dimensions were 3–5 μm thick, 20–100 μm wide, and 6 mm long. Yi *et al.* measured E to be 169.2 ± 3.5 GPa, which is close to the accepted value for the elastic modulus of macroscale SCS (169 GPa). This is expected since E is independent of size effect. The tensile strengths displayed significant dependence on the etching process, highlighting the fact that fabrication techniques should be integrated into the design process. These strength values are listed in Table IV.

Probabilistic techniques have already been used to design microscale devices. K.-S. Chen *et al.* [86, 94], in their work to design a silicon micro-gas-turbine generator (microengine), stated that the scatter of strength data measured in mechanical tests illustrated the need to use a probabilistic design approach, probably based on the Weibull statistics. The concept of microengines

generating 50 W of electrical power in a package less than 1 cm^3 in volume is based on very high speed moving parts, hence inducing high tensile stresses. In order to predict the reliability of such complex devices, strength data obtained from testing specimens produced via the same fabrication techniques and having comparable effective size as the microengine are needed. K.-S. Chen *et al.* developed and tested microfabricated biaxial flexure specimens for this purpose. The biaxial flexure specimen consisted of a square plate (10 mm $\times$ 10 mm, and 230–280 μm thick) that is simply supported over a circular hole. The specimen is loaded centrally to induce an axisymmetric biaxial stress state. K.-S. Chen *et al.* were concerned about the effect of deep reactive ion etching (DRIE) on the surface quality, and how the surface roughness varied from one region to another (for example, smooth disk surface versus rough transition region at the hub and blade roots). To characterize the local variation in surface quality and its effect on strength reduction, K.-S. Chen *et al.* developed a specimen configuration referred to as the radiused hub flexure specimen [86].

An added complication to designing with single crystal materials is how the material's elastic properties, strength, and fracture toughness vary with crystallographic orientation. For cubic crystal materials like SCS, is it necessary to conduct anisotropic stress analysis or does isotropic stress analysis provide close enough answers to warrant its use? To answer this question, K.-S. Chen *et al.* performed two types of FEA simulations for SCS biaxial flexure specimen. The first type modeled the specimen using 2-D axisymmetric analysis assuming isotropic behavior with $E = 170$ GPa and $\nu = 0.1$, which are the equivalent isotropic material constants for polycrystalline silicon. The second type modeled the specimen using 3-D analysis and used the anisotropic cubic elastic constants of SCS. Results indicated that the stresses for the two models are within 3%. Based on these results they justified using 2-D isotropic analysis for SCS to model the stress state in the biaxial flexure specimens.

In their study, K.-S. Chen *et al.* [86] found the Weibull characteristic strength to range between 1.2 GPa for the mechanically polished and 4.6 GPa for the DRIE SCS biaxial flexure specimens. The Weibull moduli also varied with the processing technique ranging between 3 and 12. Such low Weibull moduli values further support the notion that MEMS design be based on probabilistic techniques.

4.2. SCS delayed failure due to slow crack growth and creep

Few studies exist in the literature regarding the delayed failure behavior of SCS at room and high temperatures. In general, various researchers have made contradictory statements with some of them stating that SCG in SCS material does not exist while others asserting that it does.

C. Chen and Leipold [95] investigated the SCG behavior and effect of proof testing in {100} SCS wafers. They were interested in utilizing proof testing to eliminate the weak parts from a given batch of wafers, yet concerned about the effect of SCG on the remaining strength of surviving parts. To evaluate these phenomena they performed biaxial flexure strength testing on chemically polished SCS wafers having 50 mm diameters and 0.33 mm thicknesses. Dynamic fatigue testing [96] was used to evaluate whether SCG exists in this material. C. Chen and Leipold's results indicated that at room temperature, SCG did not exist, since no strength degradation was detected as a function of stressing rate. This supported the validity of proof testing since the survived parts would not incur any damage during that process.

T.-J. Chen and Knapp [97] conducted stress corrosion experiments on SCS bars that were precracked with a Knoop indenter and statically tested in four-point bending. Various liquids were used to wet the surface of the beam, including water. The beams were monitored for up to two weeks and no beams failed. T.-J. Chen and Knapp, therefore, concluded that stress corrosion cracking does not take place in SCS under these conditions.

Wong and Holbrook [98] also conducted crack growth testing on precracked and indented SCS wafers. They measured the radial crack as a function of time in both ambient air and deionized water. They found that the crack did not grow. Hence, they concluded that stress corrosion crack growth did not take place because of the formation of a protective silica layer.

Conversely, Connaly and Brown [99] found that SCG does occur in SCS at a very small but measurable rate. They measured time-dependent crack growth in a precracked 75 μm long SCS cantilever beam that was excited at resonance. Crack growth changes the resonant frequency of the beam, which was correlated to crack length. Their apparatus had the capability of measuring crack growth increments on the order of nanometers over a period of weeks, translating into a crack growth rate as slow as 10^{-15} m/s. This low rate capability is significantly more sensitive than other researchers methods, allowing them to detect SCG where others might not have been able. The final rate of change in frequency correlated to a crack growth rate of approximately 2×10^{-11} m/s. This rate might be very slow for macroscopic components, but can lead to speedy failures in microscopic devices. Connaly and Brown indicated that the presence of water accelerates or initiates crack propagation in SCS. They resonated a structure in a dry air atmosphere for 1 week without crack growth. However, upon testing in humidified air crack growth took place immediately. Bhaduri and Wang [100] also observed crack growth behavior in silicon that depended on stress intensity and was many orders of magnitude higher than that measured byConnaly and Brown. Their experiments, however, involved much larger specimens.

Ando *et al.* [22] found SCS to be susceptible to cyclic fatigue loading when stressed to levels near the average fracture strength. When the tensile specimens (described earlier) where cyclically loaded at a stress ratio of 0.1 in air, three specimens cycled with maximum strains between 2.9 and 3.5% (average fracture strain =

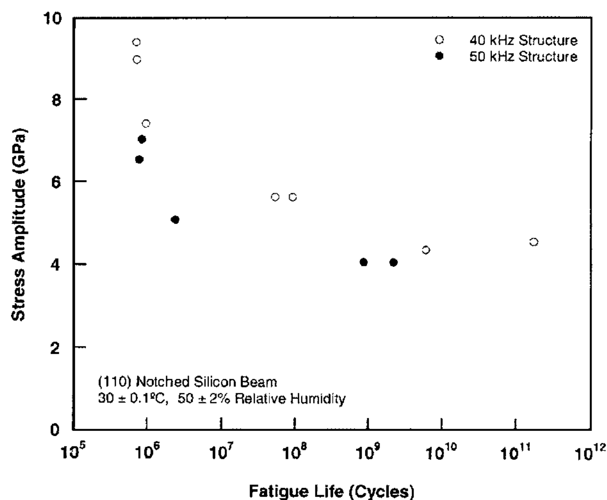

Figure 13 Stress-life curve of 20 μm thick SCS films [101].

$3.4 \pm 1.0\%$) survived over 1×10^6 cycles, and three specimens cycled with maximum strains of 3.6 and 3.7% failed in less than 100000 cycles. These data indicate that under high loads, cyclic fatigue can cause delayed fatigue failure in SCS in air at room temperature.

Fatigue tests on resonant SCS structures were performed by Muhlstein *et al.* [101] at frequencies of 40 and 50 kHz. Fig. 13 shows the S-N plot for the tested material. As can be seen from the plot, significant fatigue behavior was detected in SCS, where the fatigue strength degraded as the number of cycles increased.

SCS has a low brittle-to-ductile transition temperature (550°C) which makes it susceptible to creep at high temperature applications. For example, as has been stated earlier, MIT is developing a micro-gas turbine generator [86, 102, 103] to be fabricated from SCS. During its operation, this microengine will be exposed to creep deformation conditions in the stress range (100–200 MPa) and temperature range (600–850°C) relevant to its application [104]. Walters and Spearing [104] conducted a study to characterize the creep behavior of SCS in support of the MIT microengine project. They tested rectangular specimens under constant loading, 50 mm × 9 mm, in 4-point bend configuration. The beams were cut from 1 mm thick {100} SCS wafers, and oriented along the ⟨110⟩ crystallographic direction. A previous study by K.-S. Chen [105] investigated the temperature dependence of strength along the ⟨110⟩ direction. Walters and Spearing found the creep response under the 4-point bending condition consisted of the formation of creeping plastic hinges under the inner loading points. This macroscopic observation was consistent with the microscopic observation of increased slip band densities along the {111} planes at the inner load locations. They stated that this creep localization could have significant impact on the design of MEMS for high temperature applications.

5. Mechanical behavior of silicon nitride (Si_3N_4)

Silicon nitride is used in the microelectronics industry as a final protection layer because it is hard and scratch resistant, and can act as a sodium and moisture barrier. Currently, Si_3N_4 is being used to fabricate diaphragms and membranes used in wear resistant coating for tools, accelerometers, and pressure sensors. Si_3N_4 based MEMS devices are also used in applications where high temperature and harsh environment preclude the use of silicon-based sensors.

Few studies, in comparison with polysilicon and SCS, have been carried out to characterize the mechanical properties of silicon nitride thin films. For silicon nitride thin films, the elastic modulus has been evaluated most often (using several techniques like the bulge test, tension, bending, and resonance), followed by strength, and Poisson's ratio.

Coles *et al.* [106] used the Johns Hopkins tensile test [107] to characterize the micromechanical properties of Si_3N_4 films. To fabricate the tensile specimens, which were 4 mm long × 0.6 mm wide × 0.5 μm thick, the Si_3N_4 films were deposited on silicon wafers by LPCVD. Subsequently these films were patterned to form tensile specimens suspended across an opening in the supporting silicon substrate. Results from these tensile tests are listed in Table VI, with a measured Poisson's value of 0.23 ± 0.02. The Weibull modulus was measured to be 6.9, indicating significant scatter in strength and again pointing to the necessity of adopting probabilistic design methods.

Yoshioka *et al.* [108] tested the same on chip tensile specimen configuration used by Ando and Sato [22, 92]

TABLE VI Mechanical properties of silicon nitride

Reference/date	Test	Elastic modulus (GPa)	Average strength (GPa)	Weibull modulus	Comments
Coles *et al.* [106]/00	Tension	254 ± 3	6.41 ± 1.04	6.9	10 specimens tested. Specimens are 4 mm long × 0.6 mm wide × 0.5 μm thick
Yoshioka *et al.* [108]/00	Tension	370			Specimens are 104 μm long × 46 μm wide × 0.1 μm thick
Zhang *et al.* [109]/00	Bending	202.6 ± 15.8	12.26 ± 1.69	8	33 specimens tested. Residual stress = 291 ± 56 MPa.
Cardinale *et al.* [111]/92	Bulge test	86–125	0.39–0.42		Circular membrane specimen with 1 μm thickness and 2 cm diameter.
Bromley *et al.* [112]/83	Bulge test		0.9		Circular membrane specimen with 1 μm thickness and 1 cm diameter.
Nemeth *et al.* [113]/ 01	Bulge test	274	2.6	4.7	Square membrane with 1.06 mm width and 0.2 μm thickness.

to measure the elastic modulus and fracture strain for Si_3N_4 thin films. To fabricate the specimens, they deposited a 0.1 μm thick LPCVD Si_3N_4 film on a {100} silicon wafer having a 0.1 mm thick layer of oxide on top to serve as an inter-layer. Through a series of etching steps, the tensile specimen was released and prepared for testing. They determined the elastic modulus to be 370 GPa and the average fracture strain to be 3.8%. Both values seem to be large.

Another test configuration used to study the mechanical properties of microdevices is the bending specimen. Zhang *et al.* [109] tested Si_3N_4 film beams (referred to as microbridges by Zhang *et al.*) deposited on silicon wafers. These beams, which can be thought of as double-cantilevered beams, had dimensions of 60 μm long and 0.8 μm thick. These researchers modeled the specimen configuration taking into account the flexibility of the wafer substrate, the residual stresses, and Young's modulus using FEA. They determined that taking into account the flexibility of the substrate was essential for proper computation of the elastic modulus (otherwise E would be undervalued by about 24–28%) and the residual stresses (otherwise would be overvalued by 13–38%). The strengths were computed using a closed form formula derived by Zhang *et al.* and verified via FEA.

The bulge test is one of the first techniques developed for the study of thin films [110]. Using this method, pressure is applied to a thin film that has been clamped over a circular or square opening. By observing the deformation and pressure at which the film bursts, Young's Modulus, Poisson's ratio, residual stress, and fracture stress can be computed. Cardinale *et al.* [111] used the bulge test to study the biaxial modulus ($E/(1-\nu)$), fracture strength, and residual stress in silicon nitride films. These films were deposited by plasma-enhanced chemical vapor deposition (PECVD) on {100} gallium arsenide substrates. The circular bulge membranes that Cardinale *et al.* [111] tested had 1 μm thickness and 2 cm diameter, and were pressurized to failure. Their stress-strain diagrams were used to compute the biaxial modulus and residual stresses, while the fracture stress was computed using a closed form solution. Two different film chemical compositions were studied (Table VI). The average strength for the nitrogen-rich composition was found to be 420 MPa, while that for the silicon-rich composition was 390 MPa. These strengths are very low when compared to values obtained by other investigators. Cardinale *et al.* acknowledged this observation by comparing the strength values they measured to that obtained by Bromley *et al.* [112] for silicon nitride films deposited on {100} silicon wafers. Bromley *et al.* found the strength of 1 μm thick and 1 cm diameter circular silicon nitride membranes to be 900 MPa. Cardinale *et al.* attributed this difference in strength to size effect since their specimens were larger than the specimens tested by Bromley *et al.* However, it is highly doubtful that the entire strength difference can be attributed to size effect since the size difference between the two specimen configurations (diameters of 1 cm vs. 2 cm) is small. For example, using a Weibull modulus of 7, it takes a size ratio (A1/A2) of 350 to entirely explain the strength reduction.

Nemeth *et al.* [113] characterized the probabilistic fracture strength behavior of square amorphous Si_3N_4 thin pressurized diaphragms. They used the NASA CARES/Life brittle material design code to compute the Weibull parameters for these films. Diaphragm burst test data supplied by Mitchell [32] were used for this purpose. The effect of load and geometric variation (pressure, length, and thickness) from one tested film to the other on the stochastic nature of the strength distribution was taken into account by performing different finite element stress analyses (FEA) for the various membranes. Fig. 14 shows a quarter model displaying the FEA mesh for the MEMS bulge specimen, which had an average width of 1.06 ± 0.030 mm and thickness of 0.20 μm. The FEA stress analysis incorporated the effects due to large deflection (membrane effect) and residual stresses. The two-parameter Weibull distribution, shown in Fig. 15, was used to characterize the strength distribution for these films. This characterization yielded the Weibull parameters for the silicon nitride material. The CARES/Life program was used to further characterize the Weibull behavior for this material on a per unit area basis by using fracture mechanics based multiaxial failure criteria. This was a necessary step, which enables extrapolation of experimental data to other conditions of loading, stress state, and device geometry. Otherwise, the information reported herein only pertains to the precise conditions of the experiment and cannot be used to design other thin film devices. Knowing the Weibull parameters on a per-unit-area basis for a given material enables the design of MEMS devices using that material for a specific level of failure probability. As can be seen from Table IV, the Weibull modulus was computed to be 4.7, which is low, indicating significant scatter in strength values.

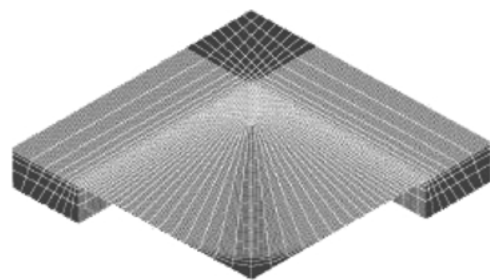

Figure 14 Quarter model showing the FEA mesh for the MEMS pressure sensor.

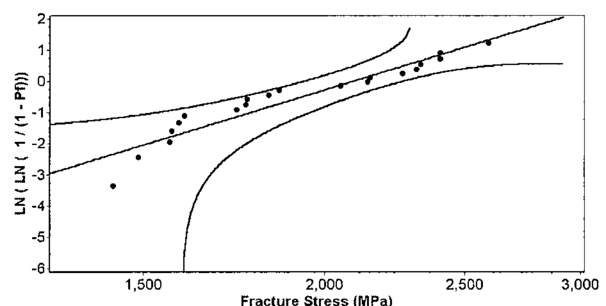

Figure 15 Weibull plot of amorphous Si_3N_4 films [113].

6. Mechanical behavior of silicon carbide (SiC)

The increasing demand for sensors to operate in harsh environments and at temperatures beyond 300°C, has led to interest in fabricating MEMS using SiC. The SiC material is desired for MEMS applications because it can be used in high temperature electronic devices including sensors for smart engines, and on-chip signal conditioning for high temperature sensors and actuators. SiC MEMS devices also possess outstanding mechanical properties such as high strength, enhanced durability, and wear resistance, which are desirable in applications such as SiC coated mechanical contacts and microfabricated bearings. During the last decade, great progress has been made in fabricating single and polycrystalline SiC films on silicon substrates.

Single crystal wafers of SiC are not suitable for MEMS, as conventional micromachining of these wafers is not yet possible [114]. However, recent developments of epitaxial and CVD growth of SiC single crystal layers (mostly cubic phase, 3C-SiC) on silicon substrate are of more interest for MEMS [114, 115]. Single crystal SiC wafers are commercially available up to 2 inches in diameter, and up to 50 μm in thickness grown on various sizes of silicon substrates [32].

Interest in poly and amorphous SiC exists because they can be processed at lower temperatures compared to single crystal SiC, and because they can be deposited on substrates other than SCS. Several fabrication methods exist for SiC. One of these methods was used by Mitchell *et al.* [32] and Yamaguchi *et al.* [42], and involves hot wall LPCVD at temperatures between 900–1050°C for polysilicon films on 3 and 4 inch silicon wafers. Other fabrication techniques involve APCVD of 3C-SiC polycrystalline films at 1000°C on polysilicon seed layers, and reactive sputtering process, which grows SiC epiaxially on oxidized silicon, layers.

Both the single and poly SiC fabrication techniques still use high temperature processing (>600°C) [114]. It has been demonstrated recently that amorphous SiC can be deposited at lower temperatures (<400°C), which makes the processing technique more compatible with IC fabrication. Many of the attractive properties of SiC are still preserved despite the lower deposition temperatures.

Table VII, which is obtained from the paper by Sarro *et al.* [114], lists the applicability of the various micromachining techniques (bulk and surface micromachining) and the possibility of using these processes for coating purposes as related to the type of SiC used (single, poly, and amorphous SiC). It can be seen that bulk micromachining can be used to fabricate devices made from all three types. However, since single crystal SiC films must be grown on single crystal silicon, surface micromachining cannot be used. On the other hand surface micromachining can be used with both poly and amorphous SiC.

TABLE VII Applicability of manufacturing technique to various SiC types [114]

SiC type	Bulk micromachining	Surface micromachining	Coating
Single crystalline	Yes	No	No
Polycrystalline	Yes	Yes	No
Amorphous	Yes	Yes	Yes

Many studies exist dealing with the elastic modulus, shear modulus, and biaxial modulus of SiC films. Mitchell [32] in his thesis reviewed and tabulated such parameters as the Young's modulus (394–457 GPa) and Poisson's ratio for bulk polycrystalline 3C-SiC, Young's modulus for bulk single crystal 3C-SiC (580 GPa in the ⟨111⟩ direction), Young's modulus for polycrystalline 3C-SiC thin films (250–360 GPa), Young's modulus for single crystal 3C-SiC thin films (295–694 GPa in the ⟨100⟩ direction), residual stresses for polycrystalline SiC films (0–250 MPa) and single crystal SiC films (0–274 MPa in the ⟨100⟩ direction). In addition, Mitchell tabulated a review of the elastic constants (compliances) and the corresponding calculated biaxial moduli for single crystal 3C-SiC in the ⟨100⟩, ⟨110⟩, and ⟨111⟩ directions and found them to range between 286–366 GPa, 385–456 GPa, and 415–482 GPa, respectively.

In this work, the review is focused on the strength of SiC films. Very few studies exist in the open literature dealing with the fracture properties of thin film 3C-SiC. Nemeth *et al.* [113], using Mitchel's data [32], characterized the probabilistic fracture strength behavior of square SiC bulge test diaphragms. Three recipes of single crystal SiC (3C-SiC) films manufactured/deposited differently, and one polycrystalline SiC film were characterized. These materials and their respective manufacturing processes were [32]:

1. Single crystal 3C-SiC (recipes 1a & 1b): For this recipe, the 3C-SiC film was grown at a rate of about 1 μm per hour at 1350°C. The difference between recipes 1a and 1b is due to the fact they were grown in two different suseptors. The thicknesses and widths for the films tested using these recipes ranged from 1.45 μm to 1.75 μm, and 1.04 mm to 1.15 mm, respectively.
2. Single crystal 3C-SiC (recipe 2): This recipe is identical to recipe 1, except that the SiC film growth rate was doubled. In both recipes the crystallographic orientations of both the silicon wafer and the SiC film are identical. The thicknesses and widths for films grown using this recipe ranged between 2.39 to 3.52 μm, and 0.995 to 1.088 mm, respectively.
3. MUSiC 1 polycrystalline SiC: If SiC growth is conducted without a carbonization step, growth temperatures between 1050°C and 1350°C result in polycrystalline films with varying sized grain sizes. In this recipe the carbonization step was skipped and a growth temperature of 1050°C was used. Thicknesses and widths for films grown using this recipe ranged between 2.50 to 3.58 μm and 0.998 to 1.076 mm, respectively.

Following the SiC growth, the SiC surfaces were polished to create a mirror finish. The backside of the wafer was also polished to remove any polycrystalline SiC growth during the growth process. For more information on the various materials and manufacturing

TABLE VIII Elastic Moduli, residual stresses and dimensions of SiC films studied in reference [113]

Material/data set	Elastic modulus (GPa)	Residual stress (MPa)	Average width (mm)	Average thickness (μm)
Recipe 1a	359	254	1.097 ± 0.041	1.60 ± 0.09
Recipe 1b	363	180	1.040 ± 0.033	1.64 ± 0.09
Recipe 2	350	120	1.049 ± 0.035	2.69 ± 0.17
Poly SiC	308	75	1.045 ± 0.038	2.86 ± 0.34

processes, reference [32] is to be consulted. The elastic moduli, residual stresses, and average dimensions for all the film materials are listed in Table VIII.

Nemeth *et al.* [113] used the NASA CARES/Life brittle material design code to compute the Weibull parameters for these films. The effect of load and geometric variation (pressure, length, and thickness) from one tested film to the other on the stochastic nature of the strength distribution was taken into account by performing different finite element (FE) stress analyses for the various films. Fig. 14, which was described earlier in the silicon nitride review section, shows a quarter model displaying the FEA mesh for the MEMS bulge specimen. The FEA stress analysis incorporated the effects due to large deflection (membrane effect) and residual stresses. Figs 16 and 17 display the Weibull strength distributions for the three single crystal SiC films, while Fig. 18 shows that for polycrystalline SiC films, respectively. These characterizations yield the Weibull parameters for the various MEMS materials. These parameters are summarized in Table IX.

Reference [113] showed how thin film strengths varied from device to device. It was also shown that device-to-device film thickness variations and suseptor-to-suseptor (manufacturing) variations were significant and must be considered in any analysis. A further ramification of this work was to illustrate the need for

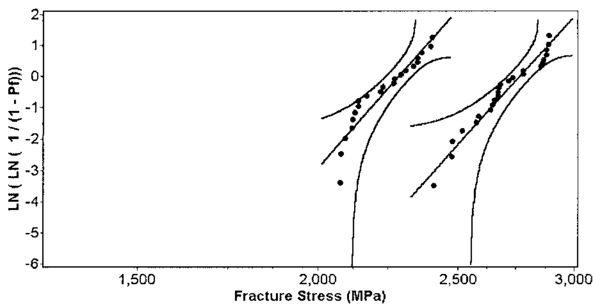

Figure 16 Weibull plot of single crystal SiC films (Recipes 1a (left) & 1b (right)) [113].

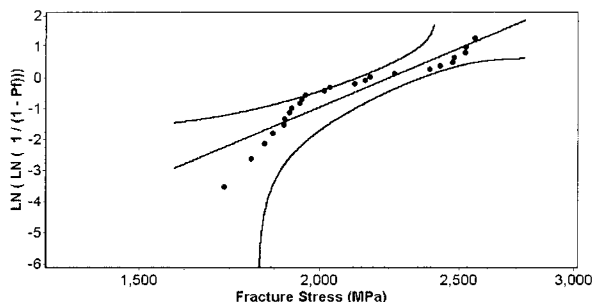

Figure 17 Weibull plot of single crystal SiC films (Recipe 2) [113].

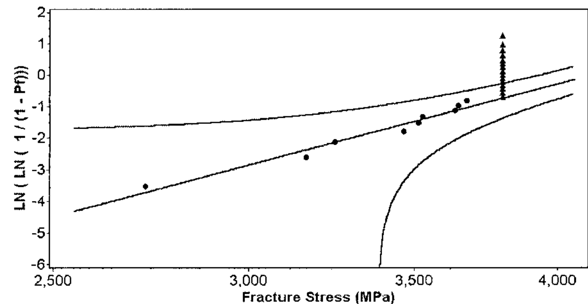

Figure 18 Weibull plot of polycrystalline SiC films. Unbroken films are denoted with the triangular points (stacked on the right) [113].

probabilistic based design practices. For a pressure sensor to be designed to survive a pressure load at a specified level of reliability, the film thickness (device geometric variations) and material processing variations must be taken into account as well as the scatter in strength observed from device to device. The design engineer needs to consider the joint probability of a device having a given thickness, with processing variations, along with the probability the material will fail due to the applied load on that device.

Windischmann [116] performed bulge testing on SiC films deposited on polished 75 mm diameter ⟨100⟩ silicon wafers using plasma enhanced chemical vapor deposition (PECVD). The free standing SiC films, up to 50 mm in diameter, were produced by back ethching the silicon. For measuring the ultimate strength, membranes 1.7–2.0 μm thick were epoxied to a fire-polished glass cylinder with a 16 mm inside diameter. The membranes had 70 MPa tensile residual stresses prior to mounting. Windischmann used an approximate closed form equation [29, 117] relating the deformation of the circular membrane to the applied pressure. This equation assumes small enough deflections so that the deflected film maintains a spherical shape, biaxial stress state uniform throughout the membrane (or at least assuming that the stress state in the central region of the film dominates), and that various higher order geometrical terms in the Taylor expansion series can be neglected. Using this equation, Windischmann computed the tensile strength to be 300 MPa. This is very low compared to the values obtained by Nemeth *et al.* Depending on how the film was epoxied to the glass cylinders, the boundary condition at the edge could range anywhere from being simply supported to being fixed end. If the bonding process maintained flexible (simply supported) conditions at the film's edge then the stress computation at the center of the film does reflect, approximately, the strength of SiC membranes. However, if the boundary condition for the film is closer to being fixed end than simply supported then the

TABLE IX Mechanical properties of silicon carbide

Reference/date	Test	Elastic modulus (GPa)	Average strength (GPa)	Weibull modulus	Comments
Nemeth *et al.* [113]/01	Bulge test	359	3.3	19.8	Recipe 1a, 21 specimens tested.
		363	4.1	22.5	Recipe 1b, 24 specimens tested.
		350	2.6	7.4	Recipe 2, 24 specimens tested.
		308	4.5	7.8	Poly SiC, 24 specimens tested.
Windischmann [116]/91	Bulge test	340–420[a]	0.3		Amorphous SiC
Jackson *et al.* [118]/02	Tension	410 ± 45	1.1 ± 0.5	2.5	3-C single crystal, tensile load along ⟨110⟩ direction
		430	0.5 ± 0.2	2.3	3-C polycrystalline

[a]Biaxial elastic modulus ($E/(1 - v)$).

highest stresses do not take place in the central region but rather at the periphery of the membrane as was found by Nemeth *et al.* [113] for the square membranes using FEA. In that case the 300 MPa value reflects the biaxial stress state at the central region of the film but not the stress at the edge of the film where failure would take place.

Recently, tensile testing of two grades of 3-C SiC was conducted by Jackson *et al.* at Johns Hopkins university [118]. One material, manufactured at Case Western Reserve University, was a single crystal film with a thickness range of 0.5–1 μm. The second material, manufactured at Massachusetts Institute of Technology, was a polycrystalline material with a thickness of 20–40 μm. The measured elastic moduli for both materials agreed well with computed values based on anisotropic elastic constants. Table IX summarizes the elastic constants, strengths and Weibull moduli for these two materials. The very low Weibull moduli measured for both of these SiC materials (2.5 and 2.3) highlight their probabilistic nature and again underscore the necessity of using probabilistic approaches when designing with these materials.

Li and Bhushan [119] used microindentation testing to measure the fracture toughness, elastic modulus and hardness of single crystal 3C-SiC films. The films, which were 3 μm thick, were deposited on ⟨100⟩ silicon substrates using APCVD. The fracture toughness was found to be 0.78 MPa·m$^{1/2}$, the hardness 25 GPa, and the elastic modulus 395 GPa. The fracture toughness of the single crystal SiC is lower than that for bulk polycrystalline SiC (around 4 MPa·m $^{1/2}$) because no grain boundaries are present to stop/deflect the propagation of cracks.

7. Conclusions

7.1. Polysilicon

Evidence exists that a Weibull size effect and significant scatter in strength are present in polysilicon MicroElectroMechanical systems (MEMS), causing them to behave similar to bulk ceramics. Weibull theory was shown to be applicable at the MEMS size scale (predicting strength of one component from that of another taking into account size and stress distribution) as long as similar materials (fabrication process, failure initiating flaws) were correlated. Polysilicon MEMS devices should be designed using probabilistic methods in order to reliably predict their short and long term behavior. Strength distributions of MEMS brittle materials (magnitude and scatter) are dependent on the fabrication process (deposition, doping, annealing, etc.), while the elastic modulus is not. Experimental evidence exists that delayed failure due to slow crack growth (SCG) in MEMS polysilicon devices can occur under both humid and dry condition. High temperature testing of MEMS remains a field seldom studied where data is very sparse and hard to come by. If MEMS devices are to be used in high temperature applications, then their mechanical properties in that thermal region must be assessed. This is necessary in order to design more reliable and durable MEMS structures.

7.2. Single crystal silicon

Single crystal silicon (SCS) exhibits significant scatter in strength and varies with the crystallographic orientation, and fabrication method of the material. Strengths ranging anywhere between 0.31 and 7.2 GPa were measured and reported by various investigators. Very few studies were found in the published literature dealing with the Weibull size effect on the strength of SCS. One exception was the study conducted by Namazu *et al.* on nano, micro, and millimeter sized bend specimens in which they found the bending strength to decrease appreciably as the specimen size increased. In general, the literature survey indicated that it is necessary to design probabilistically with this material due to the significant scatter in its strength distribution.

The elastic properties for nano, micro, and macroscale SCS parts are equivalent and display no size effect, as expected. This behavior is similar to that of polycrystalline material. In the {111} crystallographic plane, the SCS elastic properties are isotropic and hence independent of orientation.

There is contradiction in the open literature whether SCG and cyclic fatigue can take place in SCS. Some investigators detected no time dependent damage (either SCG or fatigue) in SCS at room temperature, others observed crack growth and failure under humid conditions, while others found SCS to fail due to cyclic fatigue at room temperature when subjected to high stresses. The brittle-to-ductile transition temperature for SCS is 550°C, which makes creep an important delayed failure mechanism at higher temperatures.

Very few studies were conducted at high temperatures using microspecimens. More research is needed to understand the SCG, fatigue, and creep phenomena in SCS, at elevated temperatures.

7.3. Silicon nitride

Silicon nitride exhibits significant scatter in strength which varies with the fabrication method of the material. Strengths ranging anywhere between 0.4 and 12.3 GPa were measured and reported by various investigators. Unfortunately, no studies were found in the open literature that attempted to study the effect of specimen size on the strength of silicon nitride (size effect). Nevertheless, it is necessary to design probabilistically with this material due to the significant scatter in its strength distribution.

No studies were found in the open literature that dealt with delayed failure behavior in silicon nitride thin films. There is an obvious and urgent need to conduct such investigation if silicon nitride is to be used reliably in MEMS applications.

7.4. Silicon carbide

Very few studies exist in the open literature that characterize the strength and size effect behavior for silicon carbide MEMS structures. However, two studies found in the open literature suggest that significant scatter in strength does exist in silicon carbide thin films. This behavior indicates that probabilistic treatment is necessary when analyzing and designing silicon carbide MEMS devices.

References

1. M. MEHREGANY, Introduction to MEMS-MEMS Short Course.
2. J. REITER, M. TERRY, K. BOHRINGER, J. SUH and G. KOVACS, "Thermo-Bimorph Microcilia Arrays for Small Spacecraft Docking," MEMS-Vol. 2, Micro-Electro-Mechanical Systems (MEMS)-2000, ASME, 2000.
3. N. N. NEMETH, L. M. POWERS, L. A. JANOSIK and J. P. GYKENYESI, "CARES/Life Ceramics Analysis and Reliability Evaluation of Structures Life Prediction Program," NASA/TM-2003-106316, National Aeronautics and Space Administration, 2003.
4. W. WEIBULL, "A Statistical Theory of the Strength of Materials," Ingenoirs Vetenskaps Akadanien Handlinger, No. 151, 1939.
5. R. BARNETT, C. CONNORS, P. HERMANN and J. WINGFIELD, "Fracture of Brittle Materials Under Transient Mechanical and Thermal Loading," U.S. Air Force Flight Dynamics Laboratory, AFFDL-TR-66-220 (NTIS AD-649978), 1967.
6. A. FREUDENTHAL, "Statistical Approach to Brittle Fracture," Fracture, Vol. 2: An Advanced Treatise, Mathematical Fundamentals, edited by H. Liebowitz (Academic Press, 1968) p. 591.
7. W. WEIBULL, "The Phenomenon of Rupture in Solids," Ingenoirs Vetenskaps Akadanien Handlinger, No. 153, 1939.
8. S. BATDORF and J. CROSE, *J. Appl. Mech.* **41**(2) (1974) 459.
9. S. BATDORF and H. HEINISCH, JR., *J. Amer. Ceram. Soc.* **61**(7/8) (1978) 355.
10. T. TSUCHIYA, O. TABATA, J. SAKATA and Y. TAGA, "Specimen Size Effect on Tensile Strength of Surface-Micromachined Polycrystalline Silicon Thin Films," in Proceedings of the Tenth Annual International Workshop on MEMS, 1997.
11. *Idem.*, *J. Microelectromech. Syst.* **7** (1998) 106.
12. D. LAVAN, T. TSUCHIYA, G. COLES, W. KNAUSS, I. CHASIOTIS and D. READ, "Cross Comparison of Direct Tensile Testing Techniques on Polysilicon Films," Mechanical Properties of Structural Films, ASTM STP 1413, edited by C. Muhlstein and S. Brown, American Society for Testing and Materials, 2001.
13. T. TSUCHIYA and J. SAKATA, "Tensile Testing of Thin Films Using Electrostatic Force Grip," Mechanical Properties of Structural Films, ASTM STP 1413, edited by C. Muhlstein and S. Brown, American Society for Testing and Materials, 2001.
14. W. SHARPE, JR., K. TURNER and R. EDWARDS, *Mater. Res. Soc. Symp.* **518** (1998) 191.
15. W. SHARPE, JR., B. YUAN and R. EDWARDS, *J. Microelectromech. Syst.* **6** (1997) 193.
16. W. SHARPE, JR., K. JACKSON, K. HEMKER and Z. ZIE, *ibid.* **10** (2001) 317.
17. D. LAVAN, K. JACKSON, B. MCKENZIE, S. GLASS, T. FRIEDMANN, J. SULLIVAN and T. BUCHHEIT, "Direct Tension and Fracture Toughness Testing Using the Lateral Force Capabilities of a Nanomechanical Test System," Mechanical Properties of Structural Films, ASTM STP 1413, edited by C. Muhlstein and S. Brown, American Society for Testing and Materials, 2001.
18. S. GLASS, D. LAVAN, T. BUCHHEIT and K. JACKSON, "Strength Testing and Fractography of MEMS Materials," Sandia No. 2000-0081C.
19. S. GLASS, T. BUCHHEIT and T. FRIEDMANN, "Strength Testing and Fractography MEMS materials," Presented at the 103rd Annual Meeting of the American Ceramic Society, Indianapolis, Indiana, April 2000.
20. S. GREEK, F. ERICSON, S. JOHANASSON and M. FURTSCH, *J. Micromech. Microengin.* **9** (1999) 245.
21. S. GREEK, F. ERICSON, S. JOHANSSON and J. SCHWEITZ, *Thin Solid Films* (1997) 247.
22. T. ANDO, T. YSHIOKA, M. SHIKIDA and K. SATO, "Quasi-Static and Fatigue Fracture Strength of Microsized Silicon Film Measured by On-Chip Test Method," MEMS-Vol. 2, Micro-Electro-Mechanical Systems (MEMS)-2000 ASME, 2000, p. 1.
23. J. DING, Y. MENG and S. WEN, *J. Mater. Res.* **16** (2001) 2223.
24. C. WILSON and P. BECK, *J. Microelectromech. Syst.* **5** (1996) 142.
25. C. WILSON, A. ORMEGGI and M. NARBUTOVSKIH, *J. Appl. Phys.* **79**(5) (1996) 2386.
26. S. JOHANSSON, J. SCHWEITZ, L. TENERZ and J. TIREN *ibid.* **63**(10) (1988) 4799.
27. F. ERICSON and J.-A. SCHWEITZ, *ibid.* **68**(11) (1990) 5840.
28. P. JONES, G. JOHNSON and R. HOWE, "Statistical Characterization of Fracture of Brittle MEMS Materials," in Proceedings SPIE 3880, 2000, p. 20.
29. J. BEAMS, in "Structure and Properties of Thin Films," edited by C. Neugbauer, J. Newkirk and D. Vermilyea (John Wiley and Sons, Inc., New York, 1959).
30. M. SMALL and W. NIX, *J. Mater. Res.* **7**(6) (1992).
31. J.-Y. PAN, P. LIN, F. MASEEH and S. SENTURIA, "Verification of FEM Analysis of Load-Deflection Methods for Measuring Mechanical Property of Thin Films," Technical Digest, IEEE Solid-State Sensor and Actuator Workshop, Hilton-Head, SC, 1986.
32. J. MITCHELL, Characterization of Mechanical Properties of Cubic Silicon Carbide Thin Films Deposited Onto Silicon, Master of Science Thesis, Case Western Reserve University, Cleveland, OH, 2000.
33. S. TIMOSHENKO and S. WOINOWSKY-KRIEGER, "Theory of Plates and Shells," 2nd ed. (McGraw-Hill Book Company, New York, 1959) p. 422.
34. M. ALLEN, M. MEHREGANY, R. HOWE and S. SENTUIA, *Appl. Phys. Lett.* **51** (1987) 241.
35. J. VLASSAK and W. NIX, *J. Mater. Res. Soc.* **7**(12) (1992) 3242.
36. D. MAIER-SCHNEIDER, J. MAIBACH and E. OBERMEIER, *J. Microelectromech. Syst.* **4**(4) (1992) 238.
37. C. SU, A. FEKADE, M. SPENCER and M. WITTIG, *J. Appl. Phys.* **77**(3) (1995).
38. C. SU, M. WITTIG, A. FEKADE and M. SPENCER, *ibid.* **77**(11) (1995) 5611.
39. D. HARDWICK, *Thin Solid Films* **154** (1987) 109.
40. D. YANG and T. ANDERSON, "Fracture Toughness of SiC Determined Using Nanoindentation," Information Literature from Instron Incorporated.
41. FSM Frontier Semiconductor Measurement Inc., Film Measurement System, 1631 North First Street, Suit 100, San Jose, CA 95117.

42. Y. YAMAGUCHI, H. NAGASAWA, T. SHOKI and N. ANNAKA, "Properties of Heteroepitaxial 3C-SiC Films Grown by LPCVD," Transducers '95-Eurosensors IX, Stockholm, Sweden, June 25–29, 1995, p. 190.
43. T. KAMINS and T. CASS, *Thin Sold Films* **16**(2) (1973) 147.
44. T. KAMINS, *J. Electrochem. Soc.* **127** (1980) 686.
45. S. JAYARAMAN, R. EDWARDS and K. HEMKER, *Mater. Res. Soc.* **14** (1998) 688.
46. R. BALLARINI, Y. YIN and H. KAHN, *J. Mater. Res.* **12** (1997) 915.
47. D. MAIER-SCHNEIDER, A. KOPRULULU, S. HOLM and E. OBERMEIER, *J. Micromech. Microengin.* **6** (1996) 436.
48. W. SHARPE, JR. and K. JACKSON, "Tensile Testing of MEMS Materials," in Proceedings of the Society of Experimental Mechanics, June 2000.
49. W. SHARPE, JR., K. TURNER and R. EDWARDS, *Experim. Mech.* **39** (1999) 162.
50. W. SHARPE, JR., K. JACKSON, G. COLES and D. LAVAN, "Mechanical Properties of Different Polysilicons," MEMS-Vol 2, Micro-Electro-Mechanical (MEMS)-2000, ASME, 2000.
51. J. DING, Y. MENG and S. WEN, *Chinese J. Sci. Instr.* (2000) 440.
52. M. FURTSCH, M. OFFENBERG, H. MUENZEL and J. MORANTE, "Comprehensive Study of Processing Parameters Influencing the Stress and Stress Gradient of Thick Polysilicon Layers," in Proceedings of Micromachining Microfabrication Process Technology III, in Proceedings SPIE 3223, 1997, p. 130.
53. J. KOSKINEN, J. STEIWALL, R. SOAVE and H. JOHNSON, *J. Micromech. Microengin.* **3** (1993) 13.
54. J. BAGDAHN, W. N. SHARPE, JR. and O. JADAAN, *J. Microelectromech. Syst*. **12**(3) (2003).
55. C. MUHLSTEIN, E. STACH and R. RITCHIE, *Appl. Phys. Lett.* **80**(9) (2002).
56. S. BROWN, W. ARSDELL and C. MUHLSTEIN, "Materials Reliability in MEMS Devices," Transducers 1997, 1997 International Conference on Solid-State Sensors and Actuators, 1997.
57. C. MARXER, M. GRETILLAT, N. DE ROOIJ, R. BATTIG, O. ANTHAMATTEN, B. VALK and P. VOGEL, *Sens. Actuators* **A61** (1997) 449.
58. R. BALLARINI, The Role of Mechanics in Microelectromechanical Systems (MEMS) Technology, AFRL-ML-WP-TR-1998-4209, Air Force Research Laboratory: Dayton, Ohio, 1998.
59. H. KAPELS, R. AIGNER and J. BINDER, *IEEE Trans. Electron. Dev.* **47** (2000) 1522.
60. J. BAGDAHN and W. N. SHARPE, JR., "Reliability of Polysilicon Under Long-Term Cyclic Loading," 15th IEEE Int. Conf. on MEMS, January 20–24, Las Vegas, 2001, p. 447.
61. W. VAN ARSDELL, Subcritical Crack Growth in Polysislicon MEMS, Ph.D. Dissertation, MIT, Cambridge, MA, 1997.
62. K. JACKSON, T. BUCHHEIT and D. LAVAN, "Fracture Toughness of Thin Film Polysilicon Used in MEMS Devices," in MEMS: Mechanics and Measurements, Society of Experimental Mechanics Symposium, 2001, p. 11.
63. W. SHARPE, B. YUAN and R. EDWARDS, *Mater. Res. Soc. Symp.* **505** (1997) 51.
64. H. KAHN, N. TAYEBI, R. BALLARINI, R. MULLEN and A. HEUER, *Sens. Actuators* **82** (2000) 274.
65. R. BALLARINI, H. KAHN, N. TAYEBI and H. HEUER, "Effects of Microstructure on the Strength and Fracture Toughness of Polysilicon: A Wafer Level Testing Approach," Mechanical properties of Structural Films, ASTM STP 1413, edited by C. Muhlstein and S. Brown, 2001.
66. J. BAGDAHN, J. SCHISCHKA, M. PETZOLD and W. N. SHARPE, JR., "Fracture Toughness and Fatigue Investigations of Polycrystalline," in Proceedings of the SPIE 4558 (Reliability, Testing, and Characterization of MEMS/MOEMS), San Francisco, October 2001, p. 159.
67. A. MICHALICEK, D. SENE and V. BRIGHT, "Advanced Modeling of Micromirror Devices," in international Conference on Integrated Micro/Nanotechnology for Space applications, 1995, p. 214.
68. H. KAHN, M. HUFF and A. HEUER, *Mater. Res. Soc. Symp.* **518** (1998) 33.
69. M. EBY, W. SHARPE and G. COLES, "Mechanical Properties of Polysilicon between 0°C and 250°C," in MEMS: Mechanics and Measurements, Society of Experimental Mechanics Symposium, Portland, Oregon, 2001, p. 16.
70. J. CHAE, J-Y. LEE and S. KANG, "Measurement of Thermal Expansion Coefficient of Poly-Si Using Microgauge Sensors," in Proceedings SPIE (1997) Vol. 3242, p. 202.
71. F. JENSEN, M. MACHONKIN, N. PALMIERI and D. KUHMAN, *J. Appl. Phys.* **62** (1987) 4732.
72. J. KOHLER, K. JONSSON, S. GREEK and L. STENMARK, *J. Electrochem. Soc.* **147**(12) (2000) 4683.
73. S. TIMOSHENKO and S. WOINOWSKY-KRIEGER, *Theory of Plates and Shells*, 2nd ed. (McGraw-Hill Book Company, New York, 1959) p. 197.
74. M. VARIAM, "Behavior of MOEMS Package (TI DMD) Under Mechanical and Thermal Loads," in MEMS-Vol 2, MEMS-ASME2000, 2000.
75. J. BAGDAHN, A. PLOESSL, M. WIEMER and M. PETZOLD, "Measurement of the Local Strength Distribution of Directly Bonded Silicon Wafers Using the Micro-Chevron-Test," in Proc. 5th International Symposium on Semiconductor Wafer Bonding, Electrochemical Society PV 99-35, 2001.
76. M. PETZOLD, H. KNOLL and J. BAGDAHN, "Strength Assessment of Wafer-Bonded Micromechanical Components Using the Micro-Chevron-Test," in Proceedings of the SPIE 4558 (Reliability, Testing, and Characterization of MEMS/MOEMS), San Francisco, October 2001, p. 133.
77. J. BAGDAHN and M. PETZOLD, *J. Microsystem Techn.* **7**(4) (2001) 175.
78. J. BAGDAHN, M. BERNASCH, and M. PETZOLD, "Influence of Frequency on the Fatigue of Directly Wafer-Bonded Silicon," 8th. Int. Congress on Fatigue, Stockholm, Sweden, 2002, p. 2245.
79. A. G. EVANS and E. R. FULLER, *Metall. Trans.* **5** (1974) 27.
80. J.-A. SCHWEITZ and F. ERICSON, *Sens. Actuators* **74** (1999) 126.
81. S. WOLF and R. TAUBER, "Silicon Processing for the VLSI era," Process Technology, Vol. 1 (Lattice Press, Sunset Beach, CA, 1986) p. 5.
82. R. SHULTZ, M. JENSEN and R. BRADT, *Intern. J. Fract.* **65** (1994) 291.
83. C. CHEN and M. LEIPOLD, *Bull. Amer. Ceram. Soc.* **59** (1980) 469.
84. J. NYE, "Physical Properties of Crystals," Chapt. VIII (Clarendon Press, Oxford, 1957).
85. W. BRANTLEY, *J. Appl. Phys.* **44**(1) (1973).
86. K.-S. CHEN, A. AYON and S. SPEARING, *J. Amer. Ceram. Soc.* **83**(6) (2000) 1476.
87. T. TSAKALAKOS, *Thin Solid Films* **75** (1981) 293.
88. S. HU, *J. Appl. Phys.* **53** (1982) 3576.
89. R. EISNER, *Acta Metall.* **3** (1955) 414.
90. G. PEARSON, W. READ, JR. and W. FELDMANN, *Acta Metall.* **5** (1957) 181.
91. T. NAMAZU, Y. ISONO and T. TANAKA, "Nano-Scale Bending Test of Si Beam for MEMS," in Proceedings IEEE Thirteenth Annual International Conference on Micro Electro Mechanical Systems, 2000, p. 205.
92. K. SATO, T. YOSHIOKA, T. ANDO, M. SHIKIDA and T. KAWABATA, *Sens. Actuators* A **70** (1998) 148.
93. T. YI, L. LI and C.-J. KIM, *Sens. Actuators* **83** (2000) 172.
94. K.-S. CHEN, S. SPEARING and N. NEMETH, *AIAA Journal* **39**(4) (2001) 720.
95. C. CHEN and M. LEIPOLD, *J. Amer. Ceram. Soc.* **68**(2) (1985) C54.
96. J. RITTER and J. HUMENIK, *J. Mater. Sci.* **14**(3) (1979) 626.
97. T.-J. CHEN and W. KNAPP, "The Fracture of Single-Crystal Silicon Under Several Liquid Environments," *J. Amer. Ceram. Soc.* **63** (1980) 225.
98. B. WONG and R. HOLBROOK, *J. Electrochem. Soc.* **134** (1987) 2254.
99. J. CONALLY and S. BROWN, *Science* **256** (1992) 1537.
100. S. BHADURI and F. WANG, in "Fracture Mechanics of Ceramics" (Plenum Press, 1983) p. 327.

101. C. MUHLSTEIN, S. BROWN and R. RITCHIE, *J. Microelectromech. Syst.* **10**(4) (2001) 593.
102. A. EPSTEIN and S. SENTURIA, "Macro Power From Micro Machinery," *Science* **276**(5316) (1997) 1211.
103. S. SPEARING and K.-S. CHEN, *Ceram. Engin. Sci. Proc.* **18**(4) (1997) 11.
104. D. WALTERS and S. SPEARING, *Scripta Mater.* **42**(8) (2000) 769.
105. K.-S. CHEN, Ph.D. Thesis, Massachusetts Institute of Technology, 1999.
106. G. COLES, W. SHARPE, JR. and R. EDWARDS, "Mechanical Properties of Silicon Nitride," MEMS-Vol 2, Micro-Electro-Mechanical (MEMS)-2000, ASME 2000 (2000) p. 1.
107. W. SHARPE, JR., "New Test Structures and Techniques for Measurement of Mechanical Properties of MEMS Materials," in Proceedings of the SPIE Symposium on Microlithography and Metrology in Micromachining II, Austin, TX, 1996, p. 78.
108. T. YOSHIOKA, T. ANDO, M. SHIKIDA and K. SATO, *Sen. Actuators* **82** (2000) 291.
109. T.-Y. ZHANG, Y.-J. SU, C.-F. QIAN, M.-H. HAO and L.-Q. CHEN, *Acta Mater.* **48** (2000) 2843.
110. O. TABATA, K. KAWAHATA, S. SUGIYAMA and I. IGARASHI, *Sens. Actuators* **20** (1989) 135.
111. G. CARDINALE and R. TUSTISON, *Thin Solid Films* **207** (1992) 126.
112. E. BROMLEY, J. RANDALL, D. FLANDERS and R. MOUNTAIN, *J. Vacuum Sci. Techn.* **B1**(4) (1983) 1364.
113. N. NEMETH, O. JADAAN, J. PALKO, J. MITCHELL and C. ZORMAN, "Structural Modeling and Probabilistic Characterization of MEMS Pressure Sensor Membranes," in MEMS: Mechanics and Measurements, Society of Experimental Mechanics Symposium, Portland, Oregon, 2001, p. 46.
114. P. SARRO, *Sens. Actuators* A **82** (2000) 210.
115. G. MULLER, G. KROZ and E. NIEMANN, *Sens. Actuators* A **43** (1994) 259.
116. H. WINDISCHMANN, *J. Vacuum Sci. Techn.* A **9**(4) (1991) 2459.
117. V. PICKHARDT and D. SMITH, *J. Vacuum Sci. Techn.* **14**(3) (1977) 823.
118. K. JACKSON, G. DIRRAS, R. EDWARDS and W. SHARPE, JR., "Mechanical Properties of 3C Thin-Film Silicon Carbide," in Proceedings of the 2002 SEM Annual Conference, Milwaukee, 2002, p. 99.
119. X. LI and B. BHUSHAN, *Thin Solid Films* **340** (1999) 210.